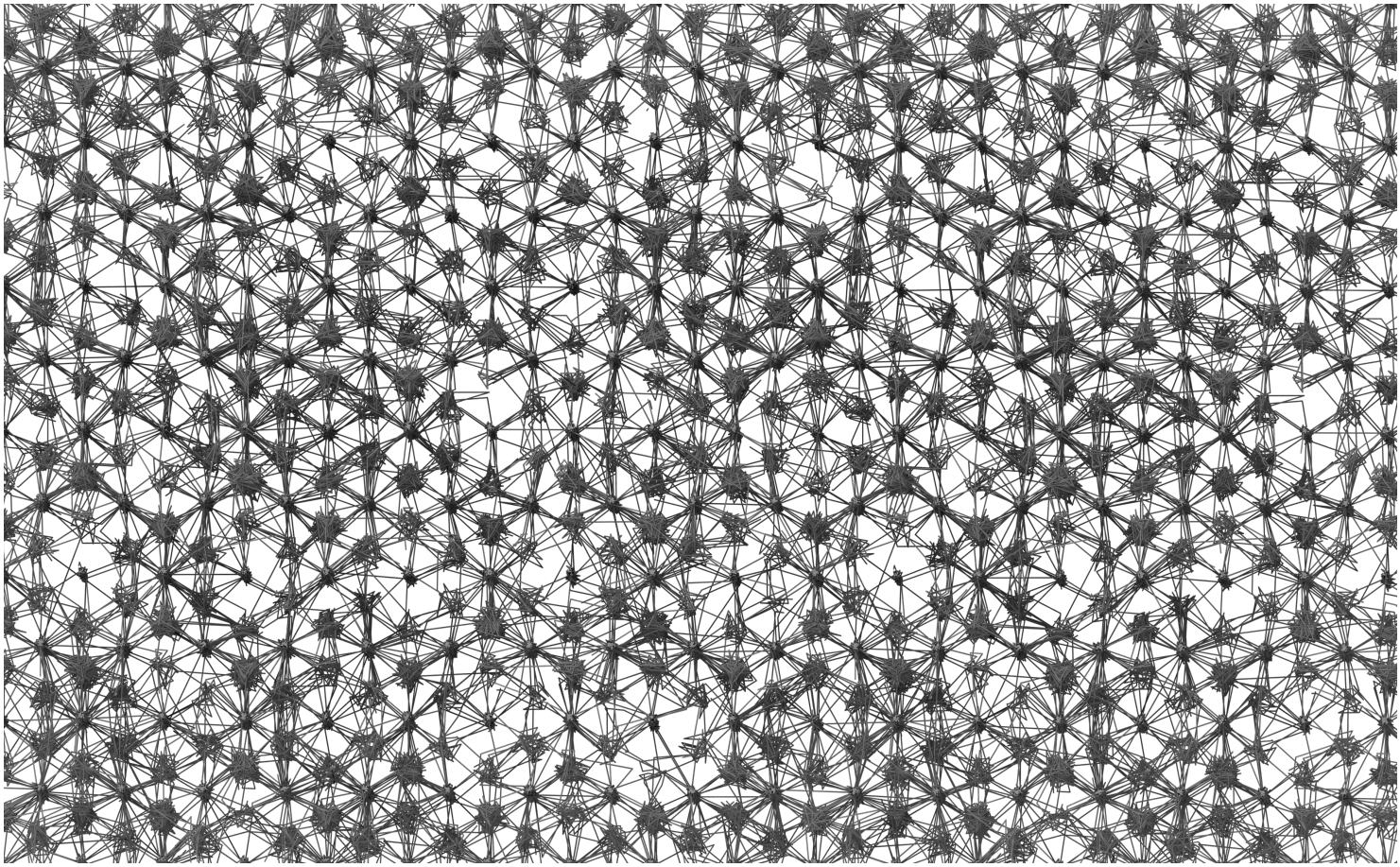

Hydrogen in Ferrite Systems with Carbide Precipitates

A Computational Investigation

Master's thesis in Physics

Felix Uddén

DEPARTMENT OF PHYSICS

CHALMERS UNIVERSITY OF TECHNOLOGY
Gothenburg, Sweden 2025
www.chalmers.se

Master's thesis 2025

Hydrogen in Ferrite Systems with Carbide Precipitates

A Computational Investigation

Felix Uddén

CHALMERS
UNIVERSITY OF TECHNOLOGY

Department of Physics
Division of Condensed Matter and Materials Theory
Computational Materials Research group
Chalmers University of Technology
Gothenburg, Sweden 2025

Hydrogen in Ferrite Systems with Carbide Precipitates
A Computational Investigation
Felix Uddén

Supervisor: Erik Fransson, Department of Physics
Examiner: Paul Erhart, Department of Physics

Master's Thesis 2025
Department of Physics
Division of Condensed Matter and Materials Theory
Computational Materials Research group
Chalmers University of Technology
SE-412 96 Gothenburg
Telephone +46 31 772 1000

Cover: Diffusion paths of hydrogen in Cr_7C_3.

Typeset in LaTeX
Printed by Chalmers Reproservice
Gothenburg, Sweden 2025

Hydrogen in Ferrite Systems with Carbide Precipitates
A Computational Investigation
of Hydrogen Trapping in Hybrid Ferrite-Carbide Systems
Felix Uddén
Department of Physics
Chalmers University of Technology

Abstract

This work investigates the behavior of hydrogen in ferritic steel, two distinct metal carbides, and hybrid ferrite–carbide systems using computational methods. A neural-network potential, trained on density functional theory data, was used to enable large-scale molecular dynamics simulations over nanosecond timescales and across a range of temperatures and compositions.

Hydrogen diffusivity was systematically investigated in ferrite structures alloyed with varying concentrations of chromium, as well as in M_7C_3 and $M_{23}C_6$-type carbides composed of different metallic species including chromium, molybdenum, vanadium, and iron. The two carbide types exhibited different diffusion behavior: M_7C_3 showed anisotropic diffusion through well-defined channels, while $M_{23}C_6$ supported more isotropic diffusion via connected site networks.

In hybrid systems combining ferrite with a spherical carbide precipitate, hydrogen was found to accumulate both at the interface and within the carbide phase. Where $M_{23}C_6$ facilitated deeper bulk trapping than M_7C_3. The simulations also revealed structural features such as the formation of a chromium-enriched shell at the carbide surface.

Keywords: hydrogen trapping, carbides, ferrite, diffusivity, molecular dynamics

Acknowledgements

I would like to thank my supervisor, and examiner, Erik Fransson and Paul Erhart for the help and guidance during my work with this thesis. Looking forward to learning more from you both during the coming years at Chalmers.

I would also like to thank my office mates for the nice conversations and every one else at the division of Condensed matter and materials theory for the nice Thursday fikas. And all other masters thesis students at the division for all fun coffee breaks and lunches.

Finally, I would like to thank all my friends and family for making my time studying at Chalmers memorable and fun despite all the difficult exams and stressful hand-ins. I am especially grateful for the support from my partner, Andrea, and for her patience in listening to all my ramblings about math and physics, which may have been neither interesting nor understandable.

Felix Uddén, Gothenburg, June 2025

Nomenclature

Below is the nomenclature of indices, sets, parameters, and variables that have been used throughout this thesis.

Used variables

c_i	Concentration of species i
k_B	Boltzmann constant
T	Temperature
ψ	Thermodynamic potential
G	Gibbs free energy
G_i	Gibbs free energy of species i
G_{Mix}	Gibbs Free energy of mixing
S	Entropy
H	Enthalpy
$\kappa,\ \phi$	Constraint variables of the VCSGC ensemble
Δt	Time step

Contents

List of Figures

List of Tables

1
Introduction

The hydrogen economy is crucial for addressing the challenges associated with transitioning from fossil fuels to renewable energy. A major hurdle to the widespread use of hydrogen as a fuel and energy storage medium is its adverse effect on metals–particularly steels–known as hydrogen embrittlement [1]. Hydrogen embrittlement occurs when hydrogen atoms intercalate into the metal lattice and, through various mechanisms, weaken the metal, causing it to fail under lower loads. This characteristic, combined with the reactive nature of hydrogen, poses significant risks for hydrogen powered vehicles, pipelines, and any structures operating in hydrogen-rich environments. Due to these challenges, hydrogen embrittlement has been extensively studied over the past decades, yet there are still unanswered questions about atomistic and nano-scale processes in these systems [2].

One strategy to mitigate hydrogen embrittlement is to introduce hydrogen traps inside materials, thereby limiting the amount of hydrogen available to participate in the embrittlement process [3]. Transition metal–based carbide precipitates have been shown to effectively trap hydrogen [4], [5]. However, the exact mechanisms governing the strength of these traps as well as the specific regions where hydrogen is trapped, remain poorly understood. This includes differences between various carbide structures and whether hydrogen can be captured and trapped within the carbide bulk or only at the interface between the precipitate and the host lattice.

To simulate these systems and characterize hydrogen behavior within them, molecular dynamics (MD) simulations can be employed. By leveraging the efficiency of machine-learned interatomic potentials, it becomes feasible to simulate systems comprising tens or hundreds thousands of atoms over nanometer-length and nanosecond-time scales [6]. This enables the investigation of complex structures and alloys. In this work, the hydrogen trapping properties of two quaternary carbides–M_7C_3 and $M_{23}C_6$, both common precipitates in steels–are studied in the context of their behavior as inclusions in a ferritic matrix [7]. The constituent metallic elements considered are chromium, iron, molybdenum, and vanadium. This is done in conjuncture with simulating the isolated systems to investigate the hydrogen diffusivity.

1.1 Aim

The aim of this project is to characterize the behavior of hydrogen in complex metal carbides and at ferrite-carbide interfaces. The key properties of interest include the hydrogen trapping capacity, diffusivity, and the spatial distribution of trapped hydrogen, at the interface between the ferrite matrix and the carbide precipitates.

1.2 Limitations

By using the GPUMD [8] package to perform MD simulation using a NEP [9] model it is possible to simulate large systems for a relatively low computational cost. Despite this the total system size, i.e., the number of atoms, is still limited. Therefor the number of atoms in the simulation, both crystal structure and hydrogen, are limited to the range 10^4 to 10^5.

Furthermore, no vacancies will be allowed in the carbon lattice. It has been shown that in some carbides vacancies in the carbon lattice increase the hydrogen trapping strength and capacity of the carbide [10]. For the two carbide structures which will be treated in this project, M_7C_3 or $M_{23}C_6$, it is not believed that vacancies have such a prominent role in the trapping behavior. They will therefor not be considered here, which in turn simplifies the simulation.

2

Metals and Hydrogen

To study hydrogen in different metals and carbides, it is essential to understand both their structures and how hydrogen contributes to their weakening. This chapter introduces the prevailing theories of hydrogen embrittlement and relates them to the structures relevant to this work. In addition, the concepts of diffusivity within a crystal structure and the thermodynamics of phase transitions are discussed.

2.1 Hydrogen embrittlement

Hydrogen embrittlement is a process in which hydrogen decreases the strength of a metal, making it brittle. The mechanisms that contribute to embrittlement have been the subject of extensive research, and the underlying mechanisms can be divided into three different processes [11], namely hydrogen-enhanced decohesion (HEDE), hydrogen-enhanced localized plasticity (HELP), and hydride formation. All three can occur simultaneously and interact in a metal exposed to hydrogen.

hydrogen-enhanced decohesion is a process that increases crack propagation in a metal. Schematically, as a crack forms, hydrogen will accumulate in and around the area due to the subsequent strain field. The surrounding metal lattice will then expand, thus weakening the bonds between metal atoms. As the metal bonds surrounding the crack region are weakened, the crack can expand more easily, promoting crack growth and causing the metal to become brittle. Typically, lattice defects, grain boundaries, and interfaces are susceptible to the HEDE mechanism.

The HELP mechanism works instead by creating localized regions where the metal has increased plasticity. This, in combination with mechanical stress, leads to the formation of micro-cavities, which in turn can lead to cracking. Such cavities can form without hydrogen, but its presence facilitates the nucleation of dislocations and hole defects, such as pores or vacancy clusters, thus exacerbating the issue.

Lastly, hydride formation is different from both the HEDE and HELP mechanisms that are caused by freely diffusing hydrogen. Hydride formation is a chemical change in the metal where hydrogen is bound by metal atoms. The embrittlement is then caused by the typical characteristics of metal hydrides, specifically, that they are, usually, more brittle than their metallic counterpart [12].

To mitigate the effects of HEDE and HELP by reducing hydrogen mobility within metal lattices, one effective strategy is to incorporate regions of metal carbides into the host lattice. This is achieved by alloying iron with various metals and carbon, promoting the nucleation and growth of carbide structures. The effectiveness of this approach relies on the presence of sites where hydrogen can be tightly bound, i.e.,

trapped, preventing it from participating in the embrittlement process [4]. There exists a vast range of possible carbide structures and compositions to explore; among them, carbides based on transition metals from group IVB to VIB have demonstrated strong hydrogen-trapping capabilities [5]. In particular, chromium-rich carbides combined with vanadium and molybdenum have been shown to significantly reduce the impact of hydrogen embrittlement [13]. Hydrogen trapping typically occurs at or near the interface between the metal carbide and the surrounding ferrite matrix, a phenomenon attributed to the strain field generated by the carbide nanoparticle [4].

2.1.1 Ferrite

Ferrite is a specific type of iron, also know as α-Fe, that has a body centered cubic (BCC) structure. In the BCC structure of ferrite, two primary hydrogen sites exist: tetrahedral and octahedral, as illustrated in Fig. 2.1. Among these, the tetrahedral site is energetically preferred [14]. Because of this preference, the energy barrier between adjacent tetrahedral sites becomes particularly important for understanding hydrogen diffusion, as it represents the dominant diffusion pathway. The barrier height for diffusion between neighboring tetrahedral sites–indicated by dashed lines in Fig. 2.1–has been calculated to be as low as 0.088 eV [14].

However, experimental measurements show significant variability due to factors such as defects and the purity of the ferrite sample. As a result, reported diffusion barriers span a broader range, from 0.035 eV to 0.14 eV. This variability is also reflected in the hydrogen diffusion coefficient in ferrite, which ranges from $3.35 \times 10^{-8}\,\mathrm{m^2 s^{-1}}$ to $2.2 \times 10^{-7}\,\mathrm{m^2 s^{-1}}$.

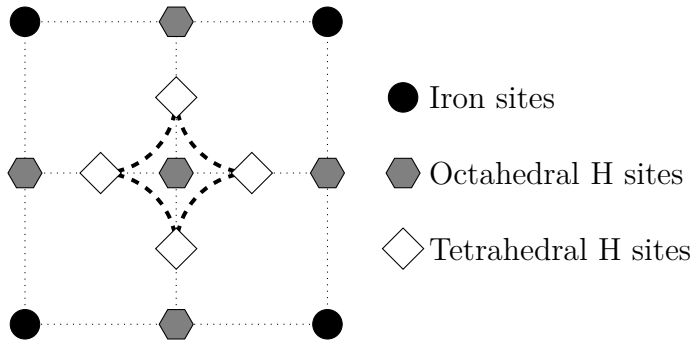

Figure 2.1: Schematic of the possible hydrogen sites in a ferrite structure, where the diffusion paths between tetrahedral is marked with dashed lines.

Ferrite systems containing chromium-rich carbides, such as those investigated in this work, will not be pure iron; instead these will be iron-chromium alloys due to the performance benefits provided by mixing chromium into the iron matrix [15]. This requires the systems to, if simulated, be created with chromium in the ferrite, or else the chromium-rich carbide will have a lower chromium level than what is experimentally observed into the larger ferrite matrix, effectively removing the possibility of trapping.

2.1.2 M_7C_3

The M_7C_3 carbide is a hexagonal structure with a unit cell (Fig. 2.2a) containing 80 atoms and belongs to the $P6_3mc$ space group [16]. The space group describes the symmetries that are present in the crystal structure. P denotes a primitive Bravais lattice, 6_3 implies that there is a symmetry along the primary axis $\langle 001 \rangle$, consisting of a six-fold rotation followed by translation of one-half of the lattice vector. The m at the second position represents that there is a mirror symmetry in planes perpendicular to the second axis $\langle 100 \rangle$, and the final c is a glide plane symmetry, i.e., mirroring and translating, along the third axis $\langle 010 \rangle$.

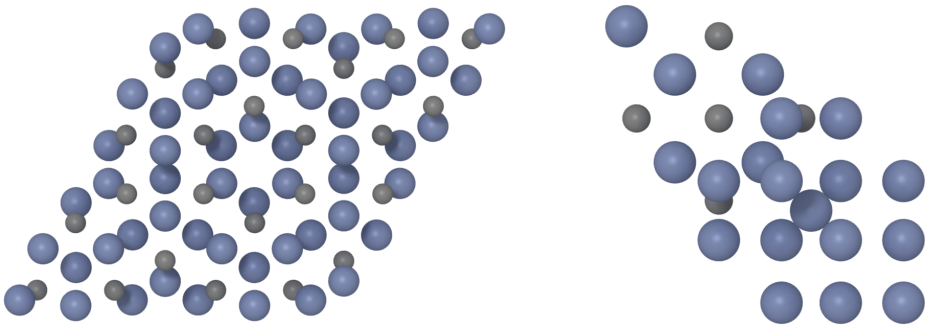

(a) M_7C_3, with $\odot z$ **(b)** $M_{23}C_6$, with $\odot z$

Figure 2.2: Unit cell for both carbides studied in this work, Cr in blue and C in gray.

M_7C_3 has been shown to work as a hydrogen trap in steels, specifically chromium-rich carbides alloyed with molybdenum and vanadium [13]. Furthermore, it has been shown to contain pathways that may allow effective hydrogen diffusion into the carbide core, which would allow for a larger number of trapping sites compared to systems where these sites are focused in the Fe-carbide interface region [6], [17]. The energy barriers through these possible pathways have been calculated with DFT and should be 0.98 eV for Cr_7C_3 and 0.72 eV in Fe_7C_3. Other barriers between hydrogen sites in the M_7C_3 carbide are on the order of 1 to 3 eV, allowing limited diffusion at room temperature [17]. However, if hydrogen is able to diffuse into the bulk of the M_7C_3 carbide, then there are hydrogen sites that are more energetically favorable than the tetrahedral sites in the ferrite matrix [4].

2.1.3 $M_{23}C_6$

$M_{23}C_6$ has a cubic structure with a unit cell (Fig. 2.2b) containing 29 atoms and belongs to the $Fm\bar{3}m$ space group [16]. From the space group; it has a face centered Bravais lattice, there is a mirror symmetry in a plane perpendicular to the principal

$\langle 100 \rangle$ and third axis $\langle 111 \rangle$, and a three-fold rotoinversion symmetry in the plane defined by the secondary axis $\langle 011 \rangle$. $M_{23}C_6$ type carbides have been shown to effectively trap hydrogen in Fe-Cr-C systems [18].

2.2 Brownian motion and diffusivity

Diffusivity is the speed with which the distribution of atoms, of a certain type, changes along a specific tensor [19]. The theoretical expression for diffusivity, the Einstein formula for Brownian motion, of an atom type can be related to the mean square displacement (MSD) in the following procedure. Consider first a crystal with principal direction x, where the diffusion of atoms A is of interest. Then let $p(\Delta x, t; x)$ be the probability that an atom of type A moves from x to $x + \Delta$ during the time t, and $n(x)$ be the concentration of atom A along x. One can then formulate the expression:

$$J_{x<x_0 \to x>x_0} = \int_{-\infty}^{x_0} n(x, t = 0) \int_{x_0 - x}^{\infty} p(\Delta x, t; x)\ d\Delta x\ dx.$$

This expression corresponds to the number of A atoms that initially were in a plane perpendicular to the x axis at $x < x_0$ and after a time t are at $x > x_0$. It is also necessary to define the reverse equation for atoms moving in the opposite direction:

$$J_{x>x_0 \to x<x_0} = \int_{x_0}^{\infty} n(x, t = 0)\ \int_{-\infty}^{x_0 - x} p(\Delta x, t; x)\ d\Delta x\ dx.$$

The difference between these two equations can then, by imposing conservation of particle number, be defined as the flux of atoms through x_0, J_x. Furthermore, also assuming that the change in concentra)tion $n(x)$ along x is slower than that of $p(\Delta x, t; x)$ along the same, it is possible to Taylor expand $n(x)$ around $x = x_0$. Thus, by partial integration, arriving at the following flux:

$$J_x = n\frac{\langle \Delta x \rangle}{t} - \frac{\langle \Delta x^2 \rangle}{2t}\frac{\partial n}{\partial x} - n\frac{\partial}{\partial x}\left(\frac{\langle \Delta x^2 \rangle}{2t}\right). \tag{2.1}$$

In a system where the atoms A are not subject to any external force fields—such as electric or magnetic fields—and the system is homogeneous aside from the spatial variation in the concentration of A atoms, it follows that $\langle \Delta x \rangle = 0$. This condition sets the first term in Eq. 2.1 to zero and reflects the absence of a preferred direction of motion; the random displacements of A atoms average out over time. Additionally, translational invariance implies that $\langle \Delta x^2 \rangle = 0$ does not depend on the absolute position in space, which leads to the vanishing of the third term in Eq.2.1. Consequently, only one non-zero term remains in the flux expression.

This remaining term involves the spatial derivative of the atomic concentration, $\frac{\partial n}{\partial x}$, and a factor that quantifies the rate at which the particles spread—namely, the diffusivity:

$$D_A = \frac{\langle \Delta x^2 \rangle}{2t}, \tag{2.2}$$

which is the Einstein relation for Brownian motion. While this derivation is presented for motion in the x-direction, analogous expressions hold for the y- and z-directions due to the isotropy of space in the absence of external fields.

However, the expression in Eq. 2.2 relating the diffusivity to the MSD does not contain any dependence on the temperature or other thermodynamic variables that describe the system. Diffusivity depends on the temperature of the system, this is related to the fact that there are energy barriers that diffusing atoms need to overcome [20]. In a thermally activated process where the diffusion can be thought of as the atom jump rate, the expression of its temperature dependence is the Arrhenius equation:

$$D(T) = D_0 \cdot e^{-E_a \beta} \quad \text{with} \quad \beta = 1/k_B T, \tag{2.3}$$

where D_0 is the diffusion prefactor, E_a is the activation energy, which depends on the barrier height between diffusion sites, T is temperature, and k_B is the Boltzmann constant. The Arrhenius equation describes the temperature dependence of diffusion well in many cases but it is not always true as there are other properties that may affect this relation. The prefactor D_0 can be expressed as:

$$D_0 = g\nu_0 l^2 \tag{2.4}$$

where ν_0 is the vibrational frequency for the hydrogen in the energy landscape of the crystal structures, l is the lattice constants, and g is a correlation factor to account for correlation between subsequent jumps [21].

2.2.1 Diffusion and temperature

The expression introduced for the diffusion coefficient assumes that the expression for the diffusivity only contains a temperature dependence of one over T in the exponent. This is, in fact, not the case as the diffusivity constant can be expressed as:

$$D_0 = gl^2\nu_0 e^{\Delta S/k_B}, \quad \text{with} \quad \Delta S = -\frac{\partial \Delta G}{\partial T} \tag{2.5}$$

where g, and ν_0 are defined as previously, with ΔS it the activation entropy, ΔG the change in free energy [22], [23]. This value ΔG incorporate the amount of energy needed to straining the lattice to allow for the diffusion. This can be related to the elastic modulus for the host material as:

$$\Delta S \approx -\mathbf{E} \cdot \frac{\mathrm{d} \ln \mu}{\mathrm{d}T}$$

with μ being the shear modulus, and $\mathbf{E}$ being defined as the heat of activation.

2.2.2 Diffusion correlation factor

To characterize the influence of hydrogen on its self, i.e., how does the hydrogen concentration affect the diffusivity, a correlation factor can be introduced. This factor, similar to that of the Haven's ratio for ionic diffusion [24], is defined as:

$$f = \frac{D}{D_{\text{tracer}}} \tag{2.6}$$

where D is the diffusivity, and D_{tracer} is the tracer-diffusivity. The difference between these two is that the tracer-diffusivity is the diffusivity of, in this case hydrogen, at very low concentrations. Thus, decreasing the possible correlation effects between hydrogen atoms.

2.3 Thermodynamics of mixing

To model alloy systems it is important to consider not only the concentrations of the different constituent elements but also wether or not these blends are stable. For investigating such properties the Gibbs free energy,

$$G = H - TS,$$

where H is the enthalpy, S is the entropy, and T is the temperature, can be used to map out the phase diagram and locate miscibility gaps [25]. Consider a binary alloy, if the Gibbs free energy of mixing, as schematically in Fig. 2.3 and explicitly in Eq. 2.7, is calculated as a function of the concentration of the constituents then it is possible to determine the most stable composition. Free energy of mixing per atom is given in the equation:

$$G_{\text{mix}}(c_A) = G_A c_A + G_B c_B + \Omega c_A c_B + k_B T \left[c_A \ln c_a + c_B \ln c_B \right], \tag{2.7}$$

where c_A and c_B are the constituent concentrations, k_B Boltzmann's constant, T the temperature, the variable Ω is defined as $\Omega = z\varepsilon$, z the number of bonds per atom, and ε the difference in energy of an A-B bond compared to the average of B-B and A-A bonds. Equation 2.7 can be interpreted as an enthalpy contribution, the first term, and an entropy contribution, the second term.

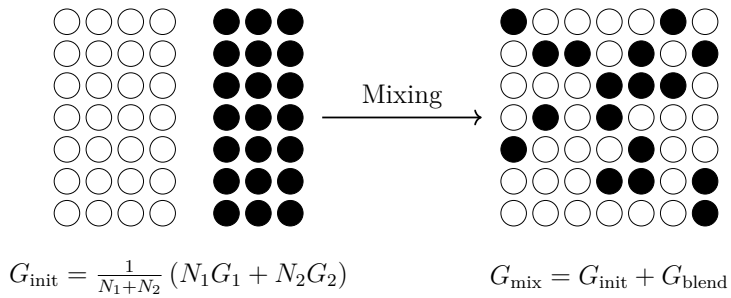

Figure 2.3: Schematic of the free energy of mixing G_{mix}, where G_{init} is the free energy of the initial system, G_{tot} is the energy of the final system as defined in Eq. 2.7, defined as the sum of the initial and any effects of mixing through G_{blend}, N_i are number of atoms of species i, and G_i is the Gibbs free energy of species i.

The excess free energy is the deviation of the free energy of mixing from the ideal case, see Fig. 2.4, this is equivalent with the parameter $\Omega \neq 0$. This implies that there are interactions between the different atoms causing different species to separate into regions rather than mix uniformly, thus, resulting in a miscibility gap in the concave region of the free energy. It is then possible to map out a phase

diagram if a tangent is drawn between the two points at the edges of this concave region for different temperatures.

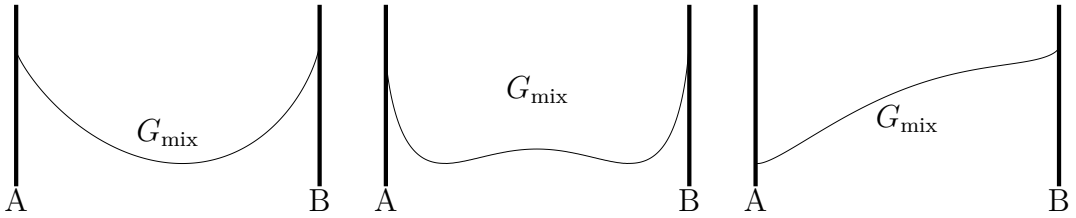

(a) $\Omega = 0,\ G_A = G_B$ **(b)** $\Omega = 0.1,\ G_A = G_B$ **(c)** $\Omega = 0.15,\ G_A \neq G_B$

Figure 2.4: Mixing energy as a function of concentration, from only A atoms to only B, at 500 K. (a) for and ideal system where the atoms have no preference of neighbors. (b) non-ideal mixing, with $\Omega = 2.5$, where the free energies per atom of the two unmixed systems are equal. (c) is non-ideal mixing here the free energy per atom of the mixed systems are different, this is the typical case when mixing a binary solution.

3
Methods

Describing thermodynamic systems and determining their properties requires a combination of theoretical approaches. In this work, DFT serves as the reference method for training a NEP model, which is then employed in MD and Monte Carlo (MC) simulations. These simulations enable the investigation of materials behavior and thermodynamic properties across a range of temperatures. The specific theoretical frameworks and methods used will be discussed in detail in this chapter.

3.1 Density functional theory

density functional theory is a computational method that has been used extensively in computational physics to determine the behavior of atoms, molecules, and materials [26]. There are several different theorems and approximations that are used in the derivation of DFT, the first of which is the Born-Oppenheimer approximation. This allows for the wave function of the entire system to be split into two parts, corresponding to electronic and nuclear degrees of freedom,

$$\Psi(\boldsymbol{r}, \boldsymbol{R}) \approx \psi(\boldsymbol{r}; \boldsymbol{R})\chi(\boldsymbol{R}),$$

where $\psi(\boldsymbol{r}, \boldsymbol{R})$ is the electron wave function for fixed nuclei position $\boldsymbol{R}$ and electron positions $\boldsymbol{r}$, and $\chi(\boldsymbol{R})$ is the nuclei wave function.

Secondly, the problem of finding the ground state for a N-electron system described by the $3N$-dimensional wave function $\psi(\boldsymbol{x}_1, \boldsymbol{x}_2, ..., \boldsymbol{x}_N)$, needs to be simplified. This is done by instead finding the energy as a function of density $\rho(\boldsymbol{r})$, dramatically reducing the complexity, for this purpose the Hohenberg-Kohn theorems are used. For the nuclear system, by Born-Oppenheimer, it can be assumed that the energy can be described as a potential energy surface.

Thirdly, the Kohn-Sham equations are used to arrive at an explicit relation between wave function, electron density, and energy. With this it is then possible to set up a self-consistency loop, see Fig. 3.1. The resulting electron density can then be used to calculate properties of interest such as energies or forces.

3.1.1 Hohenberg-Kohn theorems

The Hohenberg-Kohn theorems are fundamental to DFT, the first of two states the following, regarding an electronic system: *The external potential $v_{ext}(\boldsymbol{r})$ is determined, safe for a constant, by the electron density $\rho(\boldsymbol{r})$* [26]. Hence, as ρ determines

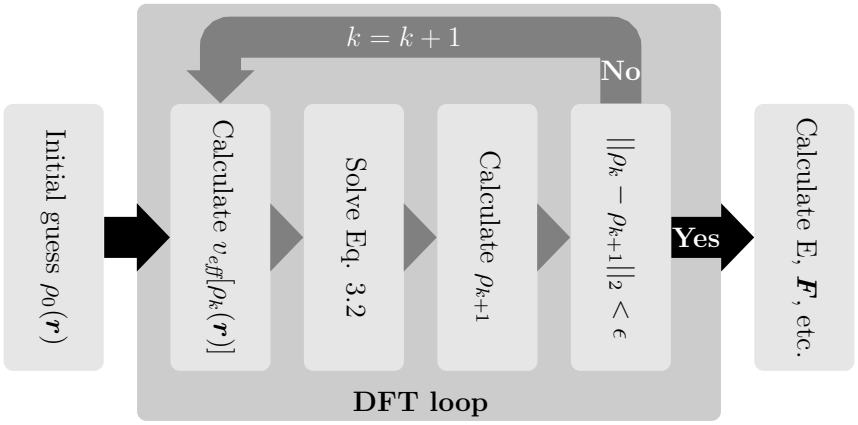

Figure 3.1: Schematic of the DFT calculation loop where, ρ_k is the electron density, calculated by Eq. 3.4, v_{eff} is the effective potential, and ϵ the maximum allowed difference between the current iterations density and the previous.

the number of electrons it also determines the ground-state wave function Ψ. This implies that the energy of an electronic system can be expressed as:

$$E[\rho] = T[\rho] + V_{ext}[\rho] + V_{ee}[\rho] \tag{3.1}$$

where T is the kinetic part; V_{ext} is the external potential; and V_{ee} is the electron-electron interaction. The second Hohenberg-Kohn theorem states that: *For any trial density* $\tilde{\rho}(\boldsymbol{r}) \geq 0 \ \forall \boldsymbol{r}$ *and* $\int \tilde{\rho}(\boldsymbol{r}) \, d\boldsymbol{r} = N$ *it holds that,*

$$E[\rho_0] \leq E[\tilde{\rho}],$$

where ρ_0 *is the ground state density.* This implies that the ground state electron density is found for the minimum energy:

$$E_0[\rho] = \min_{\tilde{\rho}} E[\tilde{\rho}].$$

By these two theorems it is possible to reformulate the N-body problem to a density problem, reducing a $3N$ dimensional problem to three dimensions. There is, however, no explicit expression that relates the energy to the electron density given by Hohenberg-Kohn theorems. This is instead given through the Kohn-Sham equations.

3.1.2 Kohn-Sham equations

To utilize the Hohenberg-Kohn theorems for DFT explicit expressions for the terms in Eq. 3.1 are needed; this is where the Kohn-Sham equations can be applied [26]. The Kohn-Sham equations assume that the original many-body problem with interacting electrons and an external potential can be represented by non-interacting particles in an effective potential. This allows the wave function to be partitioned into a product of independent functions:

$$\Psi(\{\boldsymbol{r_i}\}) = \psi_1(\boldsymbol{r}_1)\psi_2(\boldsymbol{r}_2) \cdots \psi_N(\boldsymbol{r}_N).$$

The so called orbitals ψ_i are then solutions to the Kohn-Sham equation:

$$\left[-\frac{1}{2}\nabla^2 + \underbrace{v_{ext}(\boldsymbol{r}) + v_C(\boldsymbol{r}) + v_{xc}(\boldsymbol{r})}_{=v_{eff}}\right]\psi_i(\boldsymbol{r}) = \varepsilon_i\psi_i(\boldsymbol{r}) \tag{3.2}$$

where v_{ext} is the external potential, v_C classical Columbic interaction with the nuclei, E_{xc} is the exchange-correlation term, which is a self-interaction correction, and ε_i is the eigen energy of orbital i.

The expression for the wave function allow for the energy functional to be calculated as:

$$E[\rho] = T_0[\rho] + \int d\boldsymbol{r}\rho(\boldsymbol{r})v_{ext}(\boldsymbol{r}) + E_C[\rho] + E_{xc}(\boldsymbol{r}) \tag{3.3}$$

where $T_0[\rho]$ is the kinetic energy of non-interaction particles, the integral term is the contribution of the external potential, E_C contains the classical columbic interaction energy, and E_{xc} is the exchange-correlation energy. Finally, the relation between the wave function orbitals and the electronic density is:

$$\rho(\boldsymbol{r}) = \sum_i |\psi_i(\boldsymbol{r})|^2. \tag{3.4}$$

Thus, almost all parts needed for DFT have been specified except for the exchange-correlation functional which can be approximated by using the local density approximation (LDA):

$$E_{xc}^{\mathrm{LDA}}[\rho] = \int d\boldsymbol{r}\rho(\boldsymbol{r})\varepsilon_{xc}^{\mathrm{HEG}}(\rho(\boldsymbol{r}))$$

where $\varepsilon_{xc}^{\mathrm{HEG}}(\rho(\boldsymbol{r}))$ is the exchange-correlation energy in a homogeneous electron gas.

3.2 Molecular dynamics

Molecular dynamics (MD) is a simulation method that is based on propagating a system through time by using an interaction model to determine the movement of the individual atoms. MD simulations can be used to determine the behavior of atoms in a wide range of applications. Performing a MD simulation of an atomic system, temperature, time step length, and thermodynamic ensemble, need to be selected. By choosing these variables and ensembles the simulation can be tailored to the specific aim and properties of the simulated system, the relevant ensembles for this work is introduced in the following section.

3.2.1 Micro-canonical ensemble

The NVE ensemble represents a constant number of atoms, volume, and energy. Implementing a NVE ensemble is a simpler task than that of a NPT, there is no need for any external bath and the velocity and position of any atom can be given by the velocity-Verlet integration method. This method is derived by Taylor expanding the position of each atom both forwards and backwards in time resulting in:

$$\begin{cases} \boldsymbol{r}_i(t+\Delta t) \approx \boldsymbol{r}_i(t) + \boldsymbol{v}_i(t)\Delta t + \frac{1}{2}\boldsymbol{a}_i(t)(\Delta t)^2 \\ \boldsymbol{r}_i(t-\Delta t) \approx \boldsymbol{r}_i(t) - \boldsymbol{v}_i(t)\Delta t + \frac{1}{2}\boldsymbol{a}_i(t)(\Delta t)^2 \end{cases},$$

where the backwards expansion can be shifted forward, $t = t + \Delta t$, giving an expression for the position at t:

$$\boldsymbol{r}_i(t) \approx \boldsymbol{r}_i(t + \Delta t) - \boldsymbol{v}_i(t + \Delta t)\Delta t + \frac{1}{2}\boldsymbol{a}_i(t + \Delta t)(\Delta t)^2.$$

Summing the forwards expansion and the shifted expression and solving for the velocity $\boldsymbol{v}_i(t + \Delta t)$ yields:

$$\boldsymbol{v}_i(t + \Delta t) \approx \boldsymbol{v}_i(t) + \frac{1}{2}\left(\boldsymbol{a}_i(t) + \boldsymbol{a}_i(t + \Delta t)\right).$$

This equation as well as the expression for the position can be re-formulated as functions of the force on each particle resulting in Eq. 3.5.

$$\begin{aligned} \boldsymbol{v}_i(t + \Delta t) &= \boldsymbol{v}_i(t) + \frac{\boldsymbol{F}_i(t) + \boldsymbol{F}_i(t + \Delta t)}{2m_i}\Delta t \\ \boldsymbol{r}_i(t + \Delta t) &= \boldsymbol{r}_i(t) + \boldsymbol{v}_i(t)\Delta t + \frac{1}{2}\frac{\boldsymbol{F}_i(t)}{m_i}(\Delta t)^2 \end{aligned} \tag{3.5}$$

where Δt is the time step for the MD simulation, $\boldsymbol{v}_i(t)$ and $\boldsymbol{r}_i(t)$ are the velocity and position respectively of atom i at time t, $\boldsymbol{F}_i(t)$ is the force acting on the atom, in this work predicted by a NEP model, see Eq. 3.14, and m_i the mass of the atom.

3.2.2 Isothermal-isobaric ensemble

The NPT ensemble keeps the number of atoms, pressure, and temperature constant [27]. This is achieved by having the system coupled to an external bath with a specific temperature and pressure with certain coupling strength. Using this ensemble it is then possible to study the dependence of thermodynamic and structural properties at a selected pressure and temperature.

Such a bath can be implemented computationally through a Berendsen thermo- and barostat [28]. The thermostat is implemented through the equation:

$$v_i^{\text{scaled}} = \alpha v_i \quad \text{with} \quad \alpha = \sqrt{1 + \frac{\Delta t}{\tau_T}\left(\frac{T_0}{T} - 1\right)}, \tag{3.6}$$

where v_i is the velocity of atom i, Δt is the time step for the MD simulation, τ_T is the coupling time of the thermostat, and T and T_0 are the current and target temperatures, respectively.

The barostat is implemented by using a 3×3 rescaling matrix, which scale the cell basis vectors and all positions. The rescaling matrix components, in a triclinic cell, are given by the equation:

$$\mu_{\alpha\beta} = 1 - \frac{\beta_{\alpha\beta}\Delta t}{3\tau_p}\left(p_{\alpha\beta}^{\text{target}} - p_{\alpha\beta}^{\text{instant}}\right), \tag{3.7}$$

where $\beta_{\alpha\beta}$ is the inverse of the elastic modulus, Δt is the time step for the MD simulation, τ_p is the coupling time of the barostat, $p_{\alpha\beta}^{\text{instant}}$ and $p_{\alpha\beta}^{\text{target}}$ are the current and target pressure, respectively.

The Berendsen method does not result in thermodynamically correct volume or velocity fluctuations, but it can be extended by using the stochastic cell rescaling barostat, and the Bussi-Donadio-Parrinello thermostat [29], [30]. This is achieved by changing the rescaling factor (α) for the velocity and adding an additional term for the cell rescaling ($\mu_{\alpha\beta}$). The explicit equation for the new velocity rescaling that replaces α in Eq. 3.6 is:

$$\alpha^2 = e^{-\Delta t/\tau_T} + \frac{T_0}{TN_f}\left(1 - e^{-\Delta t/\tau_T}\right)\sum_{i=1}^{N_f} R_i^2 + 2e^{-\Delta t/2\tau_T} R_1 \sqrt{\frac{T_0}{TN_f}\left(1 - e^{-\Delta t/\tau_T}\right)} \quad (3.8)$$

where Δt is the time step for the MD simulation, τ_T is the coupling time to the thermostat, T and T_0 is current and target temperature respectively, N_f is the number of degrees of freedom of the system, and $\{R_i\}_{i=1}^{N_f}$ are N_f random numbers drawn from a Gaussian distribution with zero mean and unit variance. The stochastic cell rescaling term, again for a triclinic system, that is added to the expression in Eq. 3.7 is given in Eq. 3.9 reads:

$$\mu_{\alpha\beta}^{\mathrm{SCR}} = \sqrt{\frac{2k_B T \Delta t \beta_{\alpha\beta}}{V}} R_{\alpha\beta}, \quad (3.9)$$

where $\beta_{\alpha\beta}$ is the inverse of the elastic modulus, Δt is the time step for the MD simulation, V is the current volume, k_B is the Boltzmann constant, and $R_{\alpha\beta}$ is a random number drawn from a Gaussian distribution with zero mean and unit variance. By using this combination of different baro- and thermostats it is possible to mimic the NPT ensemble more truthfully.

3.3 Monte Carlo

MC sampling is a computational method that can be used for sampling and each specific sample can be either accepted or rejected with some probability, each single instance of this is called a MC trial. This method is useful in many different areas, for crystal systems it can be used to equilibrate structures or mapping phase diagrams. When equilibrating a sample step corresponds to swapping the element of one or two atoms, depending on the selected thermodynamic ensemble. How the change is related to the probability of accepting or rejecting the change can be tailored to the specific goal of the sampling procedure. For a thermodynamic system, as the ones dealt with in this report, the acceptance probability is related to the change in thermodynamic potential. Explicitly, the acceptance probability can then be expressed as:

$$\mathcal{P} = \min\left\{1, e^{-\Delta\psi/k_B T}\right\}, \quad (3.10)$$

where $\Delta\psi$ is the change in thermodynamic potential, k_B is the Boltzmann constant, and T is the temperature of the system.

When performing MC sampling it is also possible to let the system to move between sampling. This is implemented through MCMD simulations, where a number of MC trials are performed followed by a number of MD time steps allowing the system to adjust to the new configuration. Iterating this approach the crystal is

allowed to equilibrate to its most favorable arrangement. When performing such simulations the total number of MC trials is of importance and the required number of trials depends on the size of the system, it is usually given in terms of MC cycles. One MC cycle comprises as many MC trials as there are sites.

3.3.1 Canonical ensemble

Canonical MC sampling of an atomic system will keep concentrations constant as each sample consists of swapping the species of two atoms within the system. The change in thermodynamic potential is then the difference in the potential energy of the system. In practice, this ensemble allows for an atomic structure to be equilibrated at fixed concentrations. Canonical MDMC simulation would yield the same results as a canonical MD simulation, the atoms can swap places with constant concentrations and number of atoms. This is not practically possible as the time required to simulate such a process in MD would be in the range of hundreds of thousands of years.

3.3.2 Variance constrained semi-grand-canonical ensemble

Variance constrained semi-grand-canonical (VCSGC) ensemble sampling allows, contrary to other ensembles, for the sampling of miscibility gaps by restricting the concentration mean and variance through variables κ and ϕ [31], [32]. The change in the thermodynamic potential for a system described by the VCSGC ensemble is given by Eq. 3.11.

$$\Delta\psi = \Delta E + k_B T\kappa \left(\Delta\phi_i + 2\Delta c_i + 1/N\right), \tag{3.11}$$

where ΔE is the change in potential energy, k_B is the Boltzmann constant, T is the temperature, Δc_i is the concentration change of species i, κ and ϕ_i are the variables that constrain the concentration variance and mean respectively, where $\Delta\phi_i$ is the change in ϕ_i for species i, and N is the total number of atoms in the system. For each MC trial this value is then inserted in Eq. 3.10 resulting in the swap being either accepted or rejected.

When the entire range of ϕ has been sampled the resulting concentration can be related to the change in free energy of mixing by Eq. 3.12. The free energy of mixing in a binary solution is the difference in free energy of the species being separate and when they are mixed [25].

$$\frac{\partial F_{\text{Mix}}}{\partial c_i} = -\frac{2k_B T}{N}\kappa\left(\frac{\phi_i - 2}{2} + 2\langle c_i\rangle\right) \tag{3.12}$$

The subsequent result can then be integrated along the relevant concentration axis or axes to arrive at an expression for the free energy as a function of concentrations. Furthermore, by locating regions where the free energy is concave one can locate multi-phase regions. And it is then possible to map out the phase diagram of a material as described previously in section 2.3.

3.4 Neuroevolution potential

neuroevolution potential models are a type of machine-learned interatomic potential that uses a simple feed-forward neural network with one hidden layer and a $\tanh(x)$ activation function resulting in the output in Eq. 3.13. The evolutionary part of the NEP models is that they are trained using an evolutionary algorithm, this will not be discussed further in this work [9]. The NEP model output is given by:

$$U_i = \sum_{\mu=1}^{N_{neu}} w_\mu^{(1)} \tanh\left(\sum_{\nu=1}^{N_{des}} w_{\mu\nu}^{(0)} q_\nu^i - b_\mu^{(0)}\right) - b^{(1)}, \tag{3.13}$$

where N_{neu} is the number of neurons, N_{des} are the number of descriptor components, $w^{(0)}$ and $w^{(1)}$ are the weights connecting the input to the hidden layer, and the hidden to the output layer, respectively, and $b^{(0)}$ and $b^{(1)}$ are the biases for hidden and output layers. The descriptors are the way in which the crystal structure is parametrized for the neural network input, in the NEP4 model used here these are linear combinations of Chebyshev basis functions [8], [9]. NEP descriptors consist of two different types of components: radial descriptors, components with only distance information, and many-body descriptors that depend on both distance and the relative angle between the atoms [8].

When constructing a NEP model there are multiple tuneable hyperparameters that need to be selected [8]. Firstly, the radial and angular cutoffs which determine the range of interactions that are included. Secondly, the maximum number of radial and angular descriptor components, more components may yield more accurate results at the cost of computational efficiency. Thirdly and finally, the maximum order of three, four, and five body terms, this limits the order of the spherical harmonic functions that make up the angular descriptors.

Using the NEP as an effective potential in MD simulations can then be done by relating the output U_i in Eq. 3.13 to the force on each atom. The relation between forces between atoms and NEP output can be expressed as in Eq. 3.14.

$$\boldsymbol{F}_{ij} = \frac{\partial U_i}{\partial \boldsymbol{r}_{ij}} - \frac{\partial U_j}{\partial \boldsymbol{r}_{ji}} \tag{3.14}$$

where $\boldsymbol{F}_{ij}$ is the force between two atoms i and j, $U_{i/j}$ the NEP output for the respective atoms, and $\boldsymbol{r}_{ij}$ the vector going from atom i to j.

3.5 Nuged elastic band

The NEB technique can be used to calculate energy barriers for atoms jumping between two positions by finding the minimum energy path between two configurations. By interpolating a number of states, also referred to as images, between the initial and final position, adding a spring interaction between these, and then minimizing the energy of this system the minimum energy path can be determined [33]. During this calculation only the part of the real forces perpendicular to the path, and the parallel components of the spring forces are included, see Eq. 3.15.

$$\boldsymbol{F}_i = \boldsymbol{F}_{i\,\parallel}^S + \nabla V(\boldsymbol{R}_i)_\perp \tag{3.15}$$

where $\boldsymbol{F}^{S}_{i\,\parallel}$ is the spring force parallel to the path for image i, and $\nabla V(\boldsymbol{R}_i)_{\perp}$ is the perpendicular part of the force from the potential landscape.

For diffusion the most important property is the energy barrier between initial and final configuration which is not always captured by the standard NEB approach. This is because standard NEB tends to converge to equidistant images due to all springs having the same spring constant [34]. Thus it is necessary to use a modified so-called climbing NEB method, only a slight variation to that of the initial method. By first allowing the optimization to run for a few steps and identifying the image with the highest energy. Then, the force acting on that image is changed by removing any spring forces and only allowing the force caused by the energy landscape to affect the image, both the parallel and perpendicular part. The perpendicular and parallel parts, have different signs causing the image to move towards lower potential in the direction perpendicular to the path and higher in the parallel as seen in 3.16. In this way the saddle point is captured in the calculation.

$$\boldsymbol{F}_{i_{max}} = \nabla V(\boldsymbol{R}_i)_{\parallel} - \nabla V(\boldsymbol{R}_i)_{\perp} \tag{3.16}$$

4

Computational details

Multiple different systems and the behavior of hydrogen inside them were investigated in this work. The specific systems investigated were: M_7C_3 and $M_{23}C_6$, where M are different combinations of chromium, iron, vanadium, and molybdenum, iron-chromium alloys with a BCC structure, with specific focus on Fe95%Cr5%, and combined structures consisting of a spherical inclusion of carbide inside a larger iron-chromium matrix. To prepare, run, and analyze these simulations, multiple different software packages were utilized: GPUMD [8], Calorine [35], ICET [36], ASE [37], OVITO [38], and Spglib [39]. For all MD runs, the timestep used was 0.5 fs, and all structures consisted of 45 000 atoms to 55 000 atoms, unless explixcitly specified.

4.1 Training structure generation

For training of the NEP model, multiple different structures were generated. The size of these structures was limited to approximately 20 atoms to 30 atoms, as these needed to be calculated with DFT. The structure generation for training the NEP model can be divided into three categories: carbide structures of the two crystal types, structures with hydrogen, and saddle points relevant for hydrogen diffusion in carbides.

4.1.1 Carbide mixing

The structures used to train the NEP model on carbides containing chromium and the other three relevant elements iron, vanadium, and molybdenum, were generated through groupwise enumeration of Wyckoff sites. Not all generated structures were included in the training. Instead, using the five splits of the NEP model, the energy uncertainty for each structure was quantified. All structures with an uncertainty above 5 meV/atom were selected for training the NEP model. This cutoff is not rigorously motivated but is necessary since not all structures can be included due to computational cost. This procedure was applied to both the M_7C_3 and $M_{23}C_6$ structures.

4.1.2 Hydrogen sites

When generating the structures containing hydrogen, the following procedure was used. By visual inspection, possible hydrogen sites in the unit cell of the carbides

were located. Hydrogen was placed at these sites and the entire structure was relaxed using the NEP model and CALORINE [35]. The energetically distinct hydrogen sites were then selected for training.

4.1.3 Hydrogen diffusion paths

To train the model to predict hydrogen diffusion, pairs of hydrogen sites introduced in the previous section were selected as neighbors if the distance between them was less than or equal to 2 Å. Of all pairs, those that had clear paths between them were selected, again by visual inspection, to be included in the next step. These pairs were then interpolated via the climbing NEB method and relaxed using the FIRE optimizer [40]. This was done for all enumerated structures generated previously. As this resulted in a large number of different structures, only the 35 highest-uncertainty structures for both carbide types were used in the training. For each selected structure, both the relaxed and unrelaxed structures were included. Note that not all the images from the interpolation were used—only the highest-energy structure, i.e., the saddle point.

4.2 MD simulations

All MD simulations performed in this report were done using GPUMD [8] with a NEP [9] model for the interactions. Further, data analysis was carried out using functions from the CALORINE [35] Python package. GPUMD supports multiple thermodynamic ensembles, MC sampling with different ensembles, MSD calculation, and diffusivity analysis.

4.2.1 FeCr phase diagram construction

To map out the phase diagram of the FeCr system, a pure Fe BCC structure with approximately 5000 atoms was generated. Six temperatures were selected, ranging from 300 K to 800 K in 100 K increments, and VCSGC sampling was performed for each temperature in a hybrid MDMC simulation. The variables used for the VCSGC ensemble were $\kappa = 200$, $\phi_{\mathrm{Fe}} = 0$, and $\phi_{\mathrm{Cr}} \in [-1.85, 2.3]$ with 50 equidistant points.

4.2.2 Hydrogen diffusivity

For the hydrogen diffusivity, GPUMD has implemented a MSD calculation that also yields the diffusivity. Both MSD and diffusivity are calculated for all three directions, x, y, and z. The simulations consisted of an equilibration phase, which was run for 100 ps in the NPT ensemble, followed by a longer diffusivity run of 2 ns in the NVE ensemble. During the second part, the MSD was calculated with a correlation time of 10^3 ps, allowing for multiple iterations and increased statistics.

The different, separate structure types were simulated at different temperatures; this was to ensure that all diffusivity calculations were able to converge. For the BCC iron structure, the temperatures were 900, 800, 700, and 600 K. M_7C_3 was

simulated at 900, 1000, 1100, and 1200 K. Finally, $M_{23}C_6$ was simulated at 1300, 1400, 1500, and 1600 K.

4.2.3 Hydrogen distribution at interfaces

For the simulation of hydrogen at interfaces, structures were to be generated, then equilibrated without hydrogen, which is later introduced, followed by a longer run. The structures consisted of bulk iron mixed with five percent chromium, with a spherical carbide inclusion of radius 15 Å containing of 20% Fe, 10% Mo, and 10% V. Between the carbide and iron matrix, there is a 1 Å gap which allows the structure to find energetically favorable interfaces. Equilibration of the structure was done by running 1000 canonical MDMC cycles at 500 K, without hydrogen, where all metal atoms were allowed to swap locations. The equilibrated structure was then mapped onto the initial structure with 5% hydrogen.

These equilibrated and hydrogenated structures were then allowed to run in pure MD simulations at three different temperatures: 500 K, 700 K, and 900 K. To ensure that these simulations could converge to their final states, the number of steps was determined from the MSD of hydrogen in the Fe-Cr alloy. The criterion used was that the hydrogen should be able to move through the entire structure at least 2–5 times, which resulted in the MD runs being run for 15 ns at 500 K, 700 K and 900 K.

5

Results

In this project a NEP model was trained to predict the energies and forces in three different types of structures containing iron, chromium, molybdenum, vanadium, and hydrogen. Specifically, the phase behavior of ferrite when mixing iron and chromium, the diffusion behavior in $M_{23}C_6$ and M_7C_3 type carbides with different compositions, and finally, ferrite systems with a spherical carbide precipitate with hydrogen, thus, characterizing the behavior of hydrogen in all these systems at different temperatures.

5.1 NEP model construction

The NEP model use in this work has 40 neurons in the hidden layer corresponding to a total of 14 582 parameters with radial and angular cutoffs set to 6 Å and 4 Å respectively. Only three body angular terms were included and had a maximum order of four. The maximum number of radial and angular descriptor components were set to eight and six respectively.

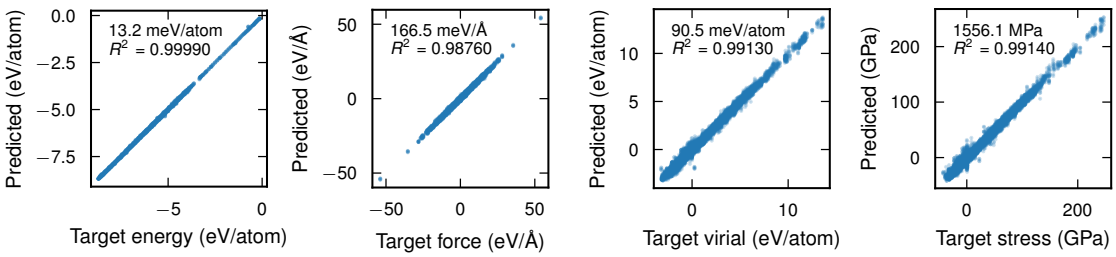

Figure 5.1: Training parity plots for the NEP model, predictions (y-axis) and DFT targets(x-axis), the root-mean-square error and R^2-score are also given in the plots.

The parity plots for the predictions of the NEP training structures after training can be seen in Fig. 5.1 together with the root-mean-square error and the R^2 score. All predicted parameters have a high R^2 above 0.99, except for the forces for which it is slightly lower. This implies that the NEP model predictions are close to their target determined by DFT calculations. Furthermore, there does not seem to be any cluster of structures for which the model performed worse compared to any other, which would have been good candidates for further training. The good performance is confirmed parity plot for the predicted and target variables in Fig. 5.2, which is somewhat worse than the training data of the test set but still of high quality.

The loss function and RMSE for the final training iteration can be seen in Fig. 5.2, where it is clear that its value has plateaued and the training has converged.

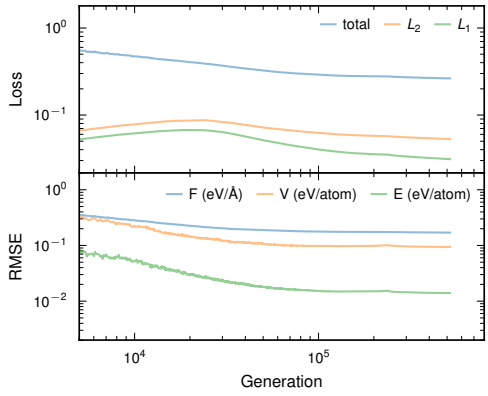

(a)

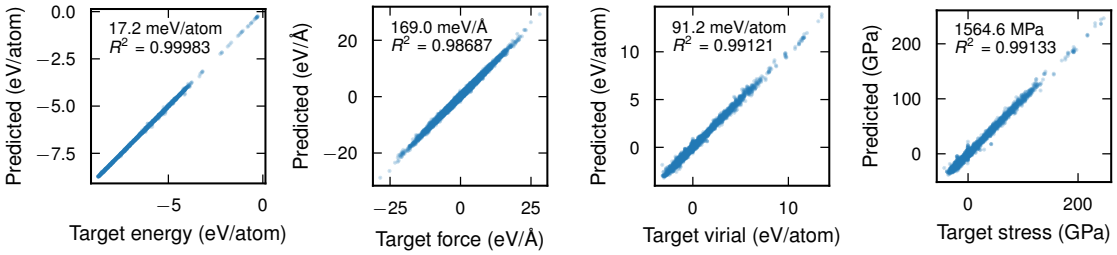

(b)

Figure 5.2: (a) Loss function and RMSE for the NEP model during the fifth training iteration. (b) Parity plot for the target and predicted variables for the test structures with the root-mean-square error and R^2-score are also given in the plots. The test structures are the training structures that were excluded from training for the specific split.

5.2 Iron-Chromium miscibility gap

Next, we investigated the phase diagram predicted by the trained NEP model in Fig. 5.3. This was done through VCSGC-MC sampling to arrive at the free energy derivative in Fig. 5.3ai. By integrating along the concentration axis the free energy was determine in Fig. 5.3aii. From the free energy the phase diagram was predicted in Fig. 5.3aii. This was done by using a convex hull construction and identifying regions where the free energy was concave. A concave shape implies that the mixing enthalpy, see Eq. 2.7, is positive. The model predicts a miscibility gap, i.e., the region with phase separation in Fig. 5.3aii, for concentration from 1-2% to 100% chromium at 300 K. At 800 K only structures with chromium concentration between 70 and 80% exhibit phase separation, and this is the maximum temperature where there is phase separation. The region is shifted to the higher concentrations of chromium for all temperatures.

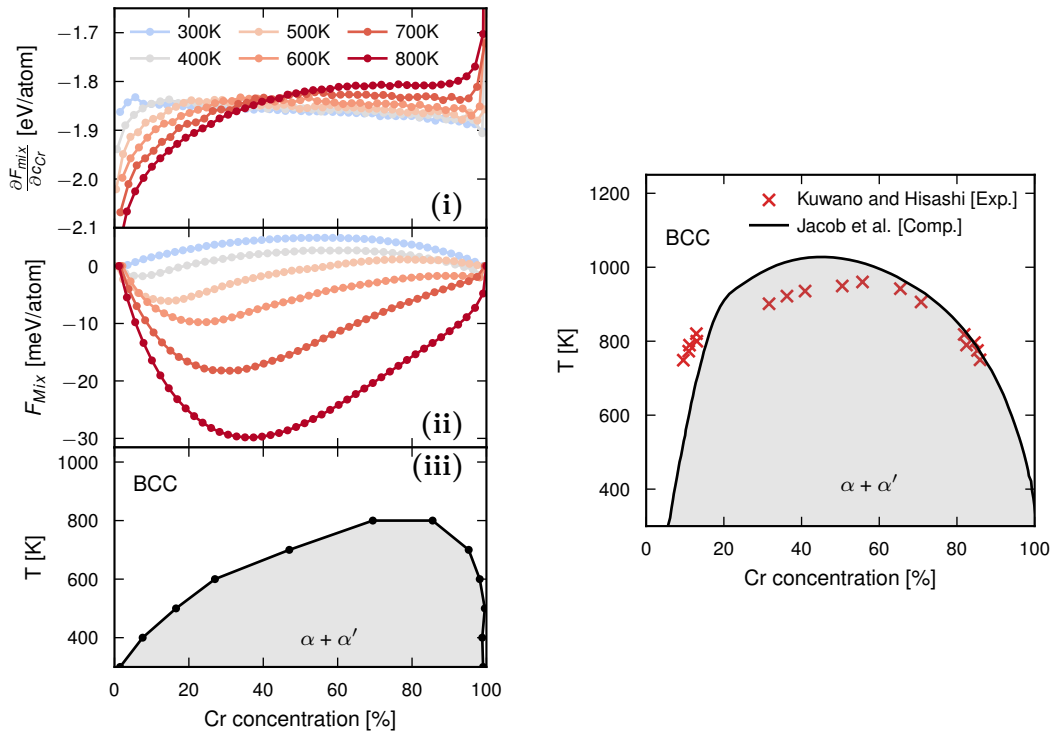

(a) **(b)**

Figure 5.3: (a) Fe-Cr phase diagram calculated through VCSGC sampling at six different temperatures is shown, where (ai) is the free energy derivative from Eq. 3.12, (aii) is the tilted free energy, (aiii) is the phase diagram for FeCr mixing. The BCC region is the region where iron and chromium mixes uniformly, in the α+α' region the two species separate into separate regions with their own structure. (b) Same system as predicted in [15], [41].

Comparing the phase prediction in Fig. 5.3a with literature data, see Fig. 5.3b, it is clear that the model correctly predicts that there is a miscibility gap iron and chromium are mixed [15]. However, it fails to capture the shape and limits of the region, both underestimating the maximum temperature and the behavior at the lower temperatures. The maximum temperature should be in the range between 900 K to 1100 K. For the lower temperatures, $\geq$400 K, between 0% and 5%, there should be a region where the two components prefer to mix, this is not reproduced in these results. The prediction is also inaccurate within the general bounds of the miscibility gap, where the highest temperature for phase separation is observed in reality at chromium concentrations around 40–50%. Although the NEP model does not capture all the specific limits of the miscibility gap, it does predict its existence, and much of the predicted region overlaps with results from both simulations and experiments.

5.3 Diffusivity in bulk ferrite and carbides

Having investigated the thermodynamic behavior of the ferrite, the next step is to add hydrogen in the bulk ferrite and carbides. These systems were investigated separately for different compositions and hydrogen concentrations. Specifically, the diffusivity of hydrogen, will be investigated and discussed in the following sections. Which may, at a later point, be used to analyze the final hybrid interface structures and to estimate the amount of time needed for the system to equilibrate.

5.3.1 Ferrite and iron-chromium mixing

The diffusivity of hydrogen in pure iron and four different iron chromium alloys, all with 5% hydrogen, can be seen in Fig. 5.4a. None of the compositions exhibits phase separation. As the chromium content increases the diffusivity in the material clearly decreases, and for all alloys the behavior is Arrhenius like. By fitting each line to the Arrhenius equation, Eq. 2.3, the diffusivity constant D_0 and activation energy E_a was determined and are presented in Fig. 5.4b together with the NEB results, calculated with the NEP and DFT, for the barrier between neighboring tetrahedral sites, and experimental results.

Firstly, the results for pure iron, both from static calculations via the NEB method and the Arrhenius fit based on MD simulations, are in rather good agreement with experimental and DFT results. The activation energy obtained from fitting the Arrhenius equation and the DFT barrier calculation are almost identical while both experimental and NEB results are slightly lower. That experimental results differ from simulations can have several causes, one of which can be related to that the hydrogen diffusivity is sensitive to crystal quality and purity. Due to this dependence on the crystal, there is a wide distribution of experimental results, typical values for the barrier range from 0.035 eV to 0.142 eV [14], a range that encompasses all four values, in Fig. 5.4b. Comparing the prefactor, the difference between the Arrhenius fit and the experimental results may seem large. However, again the typical experimental results fall in a large range, from $3.351 \times 10^{-8}\,\mathrm{cm^2 s^{-1}}$ to $2.21 \times 10^{-7}\,\mathrm{cm^2 s^{-1}}$ [14]. Thus, the results from simulations are deemed accurate. Note that the experimental results here are slightly outside the typical range; by a small margin, but it is worth noting when comparing to the remaining four alloys. A cause of the difference between NEP result and those from DFT is that the NEP model may be inadequately trained on such structures, and with further training this difference may decrease. It is worth noting that this may have little effect due to the different exchange correlation functionals used in this work being different from the literature value.

Secondly, for all other iron-chromium carbides, where there are experimental results, the difference between experimental and NEP-MD increases with the chromium proportion for E_a and is constant for D_0. The difference may be caused, as before, by both the NEP model itself or the composition of the structures not being identical. From the results for the pure iron system it is clear that the experimental values of Peñalva et al. [42] for D_0 are low relative to the typical experimental range. This could be the reason for the difference between the simulated and experimental results. What is similar, however, is that neither experiment nor simulations

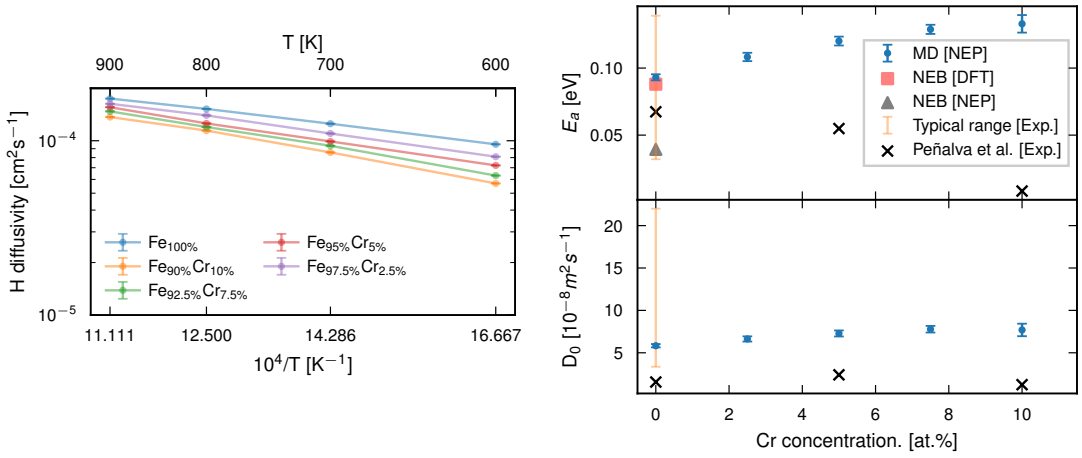

(a) **(b)**

Figure 5.4: (a) Diffusivity of of hydrogen in iron chromium alloys with varying chromium content and 5% hydrogen from MD simulations using the trained NEP model. (b) Activation energy and diffusion constant from different methods: fitting the Arrhenius equation in Eq. 2.3 to the diffusivity in (a), NEB calculation of the tetrahedral using the NEP model, DFT NEB results from [14], experimental values from [42], typical experimental range for diffusivity in pure iron [43].

show a strong dependency on the chromium content for the diffusivity prefactor of hydrogen.

Considering the results for the barrier and activation energy E_a, the results do not align very well. The experimental and simulation results do not differ greatly, but the overarching behavior as chromium content increases is not the same. By the same reasoning as previously, part of the differences can certainly be attributed to the differences in the structures; defects and impurities, specifically in the experimental material. Still, this does not explain the difference in the overall trend as chromium percentage increases, where for the experimental result show a decreasing barrier and simulations predict an increasing, and then plateauing activation energy.

Finally, although the simulation results do not align perfectly, especially for higher chromium content, most of this can be attributed to differences in the studied structure. The fact that the greatest difference occurs at the highest chromium concentration is encouraging, as all other systems examined in the following sections contain 5% chromium in the iron matrix, where the experimental and simulated results show good agreement.

5.3.2 M_7C_3

Moving on to M_7C_3 structure, in the unit cell there is a possible hydrogen pathway. The barriers of these pathways were determined by the NEB method for the four pure carbides. Each species barrier height for can be seen in Table 5.1. Comparing the NEP results with the DFT results for the Cr_7C_3 and Fe_7C_3 carbides, the NEP model slightly overestimates the values [17]. The difference is greater for Cr_7C_3

than for Fe_7C_3. This overestimation of the barrier height may be caused by differing lattice parameters, creating a structure that has less room for hydrogen than those used in the DFT results.

Comparing the NEB results with the values from MD simulations to the diffusivity in Fig. 5.6a, it is clear that the fit yields a significantly lower activation energy than the barrier calculated by NEB. This is because NEB is done in an ideal structure at zero Kelvin while the MD is done at higher temperatures. Furthermore, by performing the fit to the diffusivity in the directions of the pathways, the z direction, the activation energy is even lower. Implying that the diffusivity along the pathways is not as temperature dependent as in other directions. This is also evident from Fig. 5.6(b), where the diffusivity in the x and y directions is steeper than in the z. These results align with DFT results of the barrier of jumps outside of the pathways [17].

The mixed carbide does not, to the same extent as the pure carbides, exhibit the anisotropic behavior. The activation energy in the direction of the pathways is reduced marginally in comparison to the average. This comparatively small reduction could be explained by the different species disrupting the pathways, in fact the whole crystal structure, as they may have different lattice constants. Such a behavior is clear by studying the volume of the different structures; the volume varies from structure to structure, with iron having the lowest and molybdenum the highest, see Fig. 5.8. These differences may then lead the pathways to become less preferential compared to in the pure carbides.

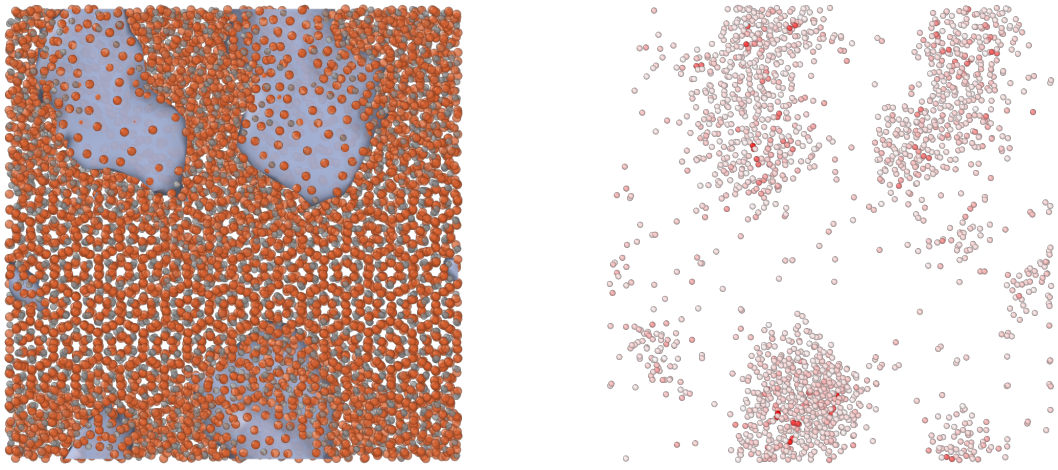

(a) Fe_7C_3 **(b)** Fe_7C_3 forces uncertainty

Figure 5.5: Hydrogen distribution in Fe_7C_3 structures at 1200 K after 5 ns in the NVE ensemble with 5% H. (a) A 10 Å thick slice of the Fe_7C_3 structure with regions containing hydrogen demarcated by the gray volumes. (b) Uncertainty, standard deviation of NEP model splits, in the force prediction for all hydrogen atoms in the same structure in (a). In (b) the color indicates the uncertainty level for each atom, where white implies low uncertainty and red corresponds to the highest value (1.24 eV/Å).

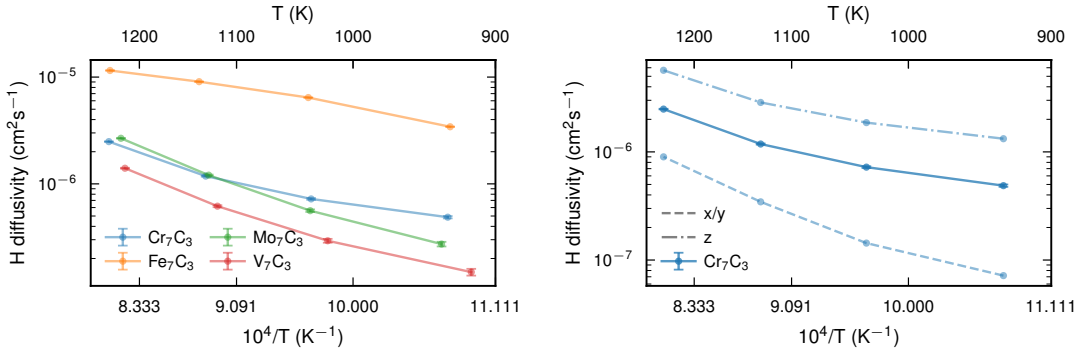

(a) **(b)**

Figure 5.6: (a) Hydrogen diffusivity in the pure M_7C_3(M=Cr, Fe, Mo or V) with 5% hydrogen from MD simulations using the trained NEP model. (b) Diffusivity in Cr_7C_3 together with the diffusivity in the three different direction x, y, and z.

Table 5.1: Barriers determined by NEB, the activation energy from fitting the data from MDto the Arrhenius equation, and the activation energy from fitting the diffusivity in the direction of the pathways to the Arrhenius equation. The M_7C_3 carbide consists of 60%Cr, 20%Fe, 10%Mo, and 10%V. All barrier values are given in eV.

Species	Cr_7C_3	Fe_7C_3	Mo_7C_3	V_7C_3	M_7C_3
NEB (DFT)[17]	0.98	0.72	—	—	—
NEB (NEP)	1.1	0.76	1.84	1.13	—
E_a (MD)	0.67	0.36	0.93	0.88	0.71
E_{az} (MD)	0.59	0.25	0.86	0.8	0.68
D_0 [10^{-4}cm^{2}s^{-1}]	13.5	3.5	175.2	60.7	25.5

In the case of M_7C_3, among the pure carbides studied, the structure exhibiting the highest hydrogen diffusivity is iron carbide, followed by chromium, molybdenum, and vanadium. While the latter three show similar diffusivity magnitudes, iron carbide exhibit significantly higher hydrogen mobility. This trend aligns with experimental observations indicating that IVB-VIB transition metal carbides are particularly effective at trapping hydrogen [5], [13]. Strong trapping abilities would affect the diffusivity negatively as there will be more sites with high barriers resulting in less frequent jumps for the diffusing hydrogen. Consequently, one would expect hydrogen diffusivity to be lower in Cr_7C_3, Mo_7C_3, and V_7C_3 compared to Fe_7C_3, consistent with their trapping capabilities.

Hydrogen behavior in Fe_7C_3 also differs qualitatively from the other carbides across all temperatures. Rather than displaying a uniform distribution along diffusion pathways, hydrogen tends to accumulate in larger, localized regions, as shown in Fig. 5.5. These regions are marked by noticeable amorphization of the surrounding crystal structure. Interestingly, this amorphization appears to depend on the total hydrogen concentration–smaller hydrogen-rich regions do not show the same struc-

tural disruption–suggesting that high hydrogen content may render the structure thermodynamically unstable. This amorphization causes the iron carbide to display different diffusion behavior compared to the other carbides. The observed behavior could stem from limitations in the NEP model, which was not trained on systems with such high hydrogen concentrations.

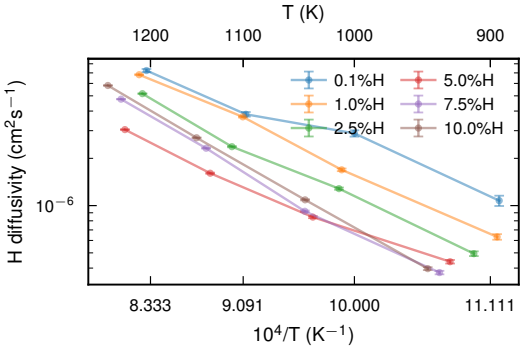

(a)

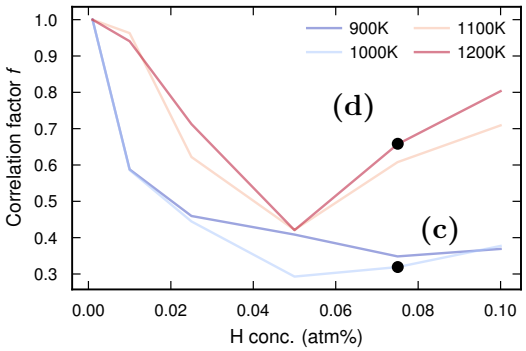

(b)

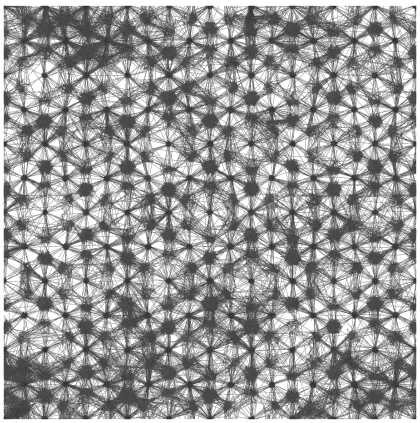

(c) 1000 K

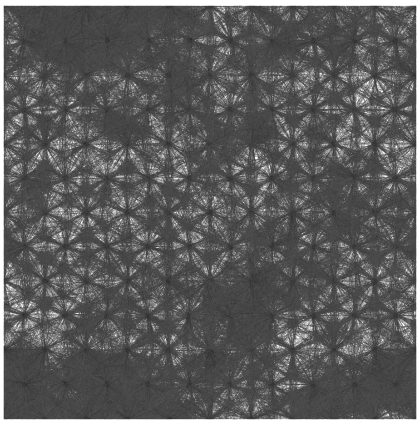

(d) 1200 K

Figure 5.7: (a) Diffusivity in the mixed M_7C_3 carbide (M=60%Cr, 20%Fe, 10%Mo, and 10%V) for four different temperatures. (b) Correlation factor f as a function of hydrogen concentration. (c), (d) Trajectories of all hydrogen atoms as they diffuse through the simulation at a two different constant temperatures, 1000 K and 1200 K. The structures in (c) and (d) are M_7C_3 (M=60%Cr, 20%Fe, 10%Mo, and 10%V) and the hydrogen concentration is 7.5%.

However, Fig. 5.5b presents the standard deviation of the predicted forces from five different NEP model splits, which indicates that the model maintains a reasonable understanding of hydrogen behavior in this system. Additionally, previous studies have reported that Fe_7C_3 exhibit lower stability than most common iron carbide Fe_3C, when considering formation enthalpy which does not account for its stability as a function of temperature [44]–[46]. This supports that the structure may show instability under high hydrogen loading at elevated temperatures.

Another property investigated is the diffusivity correlation constant f for different hydrogen concentrations, as defined in Eq. 2.6. This factor is presented in Fig. 5.7b. This shows that for the M_7C_3 structure at lower temperatures, there is a high, negative, correlation between diffusing hydrogen. This is another consequence of the hydrogen pathways, where, as the hydrogen concentration rises, the pathways fill, limiting the speed at which hydrogen can diffuse. For the higher temperatures, 1100 K and 1200 K, the correlation increases up to 5% hydrogen, where the diffusion becomes less correlated. This increase probably corresponds to the increased amount of hydrogen diffusing outside of the pathways, enabled by the increased temperature. This is supported when considering the hydrogen trajectories for the two temperatures, 1000 K and 1200 K, see Fig. 5.7(c) and (d). Here, the structure at a higher temperature supports diffusion outside the pathways, while at the lower temperature this is limited.

In Fig. 5.7a the three lowest hydrogen concentrations have some deviation from the Arrhenius plot, which is caused by the decreased statistics when calculating the MSD. Which also is why these get closer to the Arrhenius equation as the concentration rises.

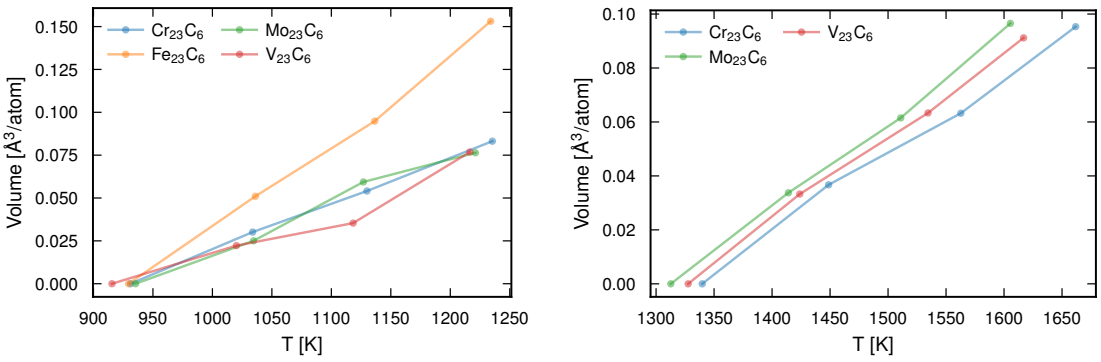

(a) M_7C_3 **(b)** $M_{23}C_6$

Figure 5.8: Thermal expansion for the four different M_7C_3 and three $M_{23}C_6$ structures investigated relative to the lowest temperature volume.

5.3.3 $M_{23}C_6$

$M_{23}C_6$ does not contain any obvious, as seen in M_7C_3, diffusion pathways that may support hydrogen diffusion. However, from Fig. 5.9a, it is clear that the structure has some sites that hydrogen can diffuse between. These sites are regularly spaced in all directions; these align with specific features in the crystal structure in Fig. 5.9b. Between these sites, there are multiple different paths that allows hydrogen to move from one region to the next. The differences between the diffusion paths in M_7C_3 and those in $M_{23}C_6$ are that the pathways in M_7C_3 are highly anisotropic, while those in $M_{23}C_6$ are cubically symmetric in all three directions. M_7C_3 mostly allows diffusion in one specific pathway structure, while the $M_{23}C_6$ structure offers many different paths; and the diffusion in $M_{23}C_6$ occurs between regions where there are a number of possible sites. These smaller regions, where there are multiple hydrogen

sites, can be seen at the intersection of the grid created by the diffusion paths of the hydrogen, see Fig. 5.9a.

As mentioned, the $M_{23}C_6$ structure has regions that hydrogen appears to prefer. This is also evident when considering the MSD. It has a clear plateau in the range between 2 ps to 20 ps for temperatures below 1200 K. The hydrogen can and does escape these sites. When leaving this specific region the hydrogen moves to one of its neighboring, and identical, regions. A process like this may facilitate the diffusion of hydrogen further into the bulk of the carbide and, by extension, allow for a large trapping capacity.

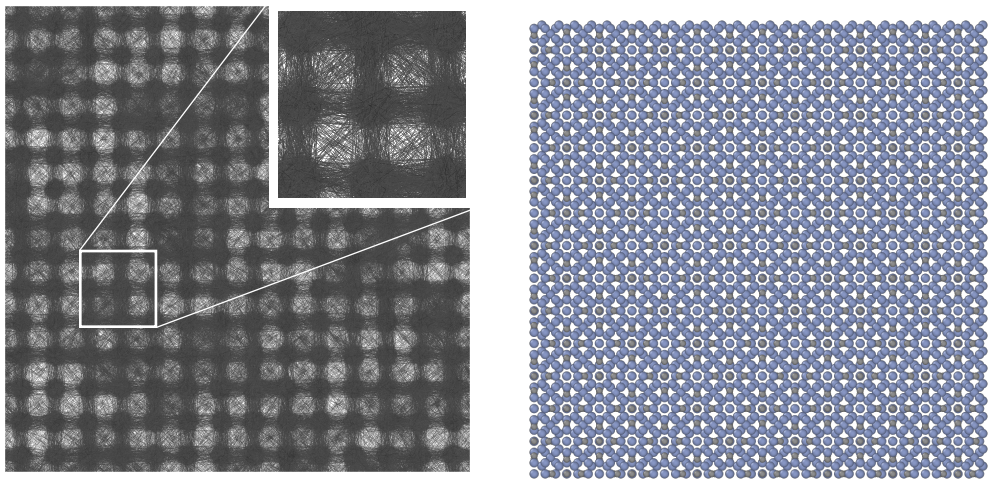

(a) **(b)**

Figure 5.9: (a) Diffusion paths for hydrogen in a $Cr_{23}C_6$ crystal at 1200 K with a hydrogen concentration of 5%, the inset displays one of these preferential regions for hydrogen. (b) Structure used in the simulation of the hydrogen diffusion in (b).

In Fig. 5.10, the diffusivity of hydrogen in the different pure $M_{23}C_6$ carbides is shown. For all pure carbides except the iron variant, the diffusivity is described by the Arrhenius equation. Both $M_{23}C_6$ and M_7C_3 have similar hydrogen diffusivity, but there are differences between the two different structures In $M_{23}C_6$, it is the molybdenum carbide that has the lowest diffusivity, and the diffusivity in $M_{23}C_6$ is on the same order as in M_7C_3.

The volume per atom for $M_{23}C_6$ is larger than that of M_7C_3 for all different carbides and temperatures, with all exhibiting similar levels of thermal expansion, exept for Fe_7C_3, see Fig. 5.8. A larger volume per atom in the structure can increase the prefactor of the diffusivity, the constant D_0. This is a result of the quadratic dependence on the lattice constant, see Eq. 2.4. Increasing the lattice constant is not the only effect of the increased volume as it also changes both ν_0 and f as well. It is then these variables that give M_7C_3 the higher prefactors.

At closer inspection of $Fe_{23}C_6$, it, like Fe_7C_3, exhibits clear amorphization at the three higher temperatures, indicating that it is not a stable structure. While Fe_7C_3 only exhibits partial amorphization in regions of high hydrogen concentration, $Fe_{23}C_6$ is completely amorphous at the higher temperatures. At the lowest

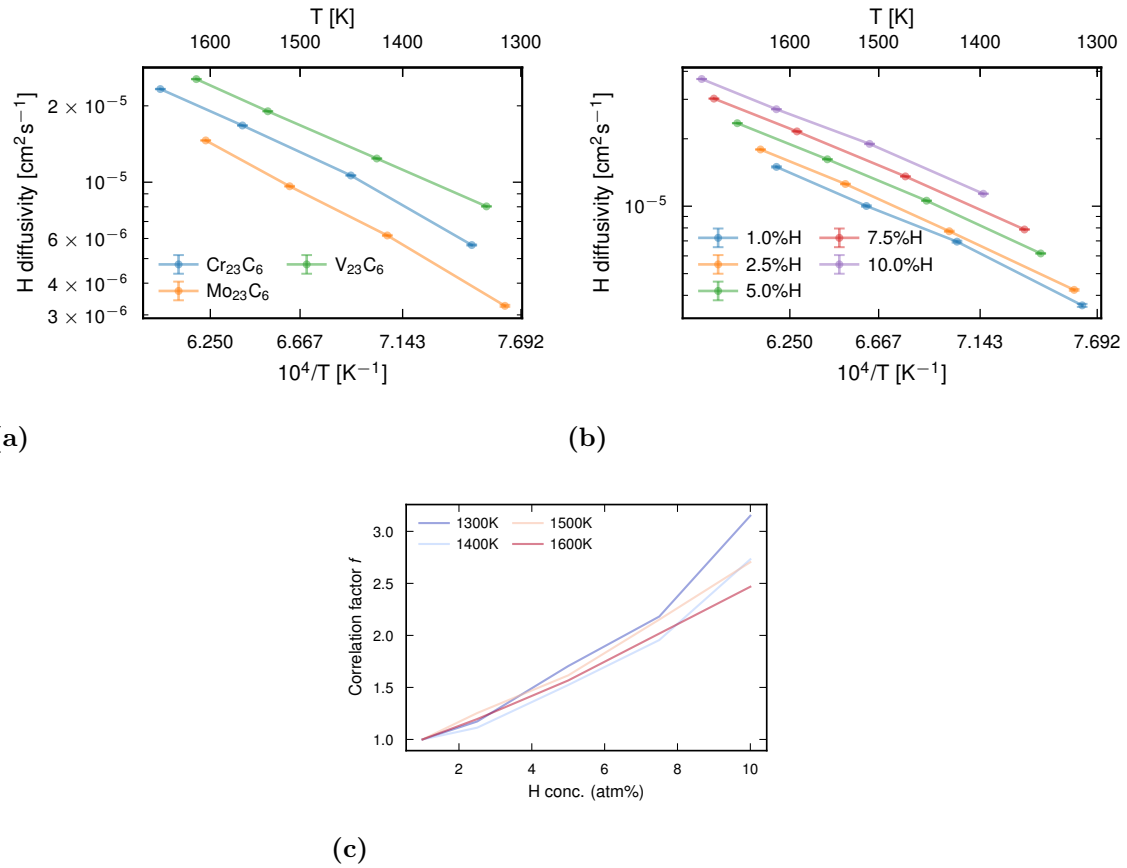

Figure 5.10: (a) Diffusivity of H in four pure $M_{23}C_6$ (M=Cr, Fe, V, and Mo) systems with H concentration of 5%. (b) Hydrogen diffusivity in $Cr_{23}C_6$ at five different hydrogen concentrations between 1 and 10%. (c) Correlation factor at four different temperatures as defined in Eq. 2.6 for the diffusivity in (b).

temperature, $Fe_{23}C_6$ does not break down, suggesting that at a lower temperature it may be meta stable. This amorphization is not present if iron is rejected but can be seen in the mixed $M_{23}C_6$ structure. If iron is removed from the $M_{23}C_6$ structure it becomes stable, i.e., iron destabilize the $M_{23}C_6$ structure which aligns with experimental results, where $Fe_{23}C_6$ type carbides have not been observed, except for in meteorites [47].

As for M_7C_3 the correlation factor was investigated for $M_{23}C_6$. Due to the instability caused by the iron component in the mixed $M_{23}C_6$ carbide, this was done for a pure $Cr_{23}C_6$ structure instead. In $M_{23}C_6$ there is a simpler correlation behavior than in the M_7C_3 structure, the diffusivity rises with the hydrogen concentration. This aligns with the observation that $M_{23}C_6$ supports multiple different diffusion paths, thus avoiding the problem in M_7C_3 where the single diffusion paths are filled. The increased hydrogen concentration could saturate the traps present in the structure allowing larger amounts of hydrogen to diffuse freely.

The difference between hydrogen correlation in M_7C_3 and $M_{23}C_6$ will impact their trapping ability. Although the M_7C_3 structures have slightly higher diffusivity than their $M_{23}C_6$ counterparts, it is reduced as the hydrogen concentration rises which

will reduce the amount of hydrogen diffusion into the carbide bulk. For $M_{23}C_6$ the opposite will be true, the more hydrogen in the carbide the easier it will be for more hydrogen to diffuse into the bulk. This may of course have negative effects on the trapping, as higher diffusivity implies worse trapping ability.

Table 5.2: Barriers determined by NEB, and activation energy from obtained via fitting to the Arrhenius equation. The $M_{23}C_6$ carbide comprises of 60%Cr, 20%Fe, 10%Mo, and 10%V.

Species	$Cr_{23}C_6$	$Fe_{23}C_6$	$Mo_{23}C_6$	$V_{23}C_6$	$M_{23}C_6$
E_a [eV]	0.8	—	0.91	0.74	—
D_0 [10^{-4}cm^{2}s^{-1}]	62.1	—	103.3	51.7	—

5.4 Interface systems with hydrogen

Adding all previous sections together, the final, combined iron-chromium/carbide systems were equilibrated at 500 K. These can be seen in Fig. 5.11. The radial distribution of atomic species for both $M_{23}C_6$ and M_7C_3, are shown in Fig. 5.12 and Fig. 5.13. These show some differences between the two carbides, both in the distribution of hydrogen and of different metallic species. The specific set of concentrations of metals were selected to enable comparison with experimental studies. In

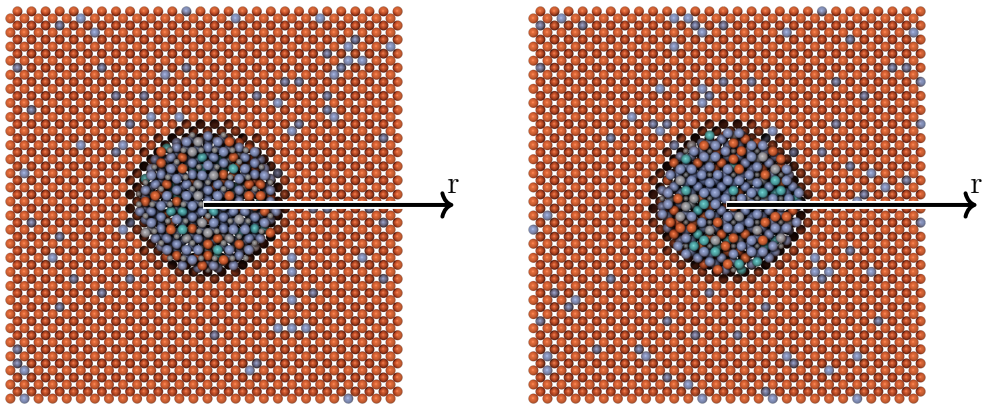

(a) M_7C_3 **(b)** $M_{23}C_6$

Figure 5.11: Interface structures, cut in half to visualize the carbide precipitate, used to simulate the behavior of hydrogen. In both (a) and (b) the definition of r used in all radial distributions is displayed. Iron atoms are orange, chromium atoms are light blue, vanadium atoms are turquoise, molybdenum atoms are gray, and carbon are small and gray.

Fig. 5.12a and b, the M_7C_3 and $M_{23}C_6$ structures are shown after equilibration at a temperature of 500 K. The distribution of metal species in the two cases does not differ significantly; however, there are some minute differences and some similarities worth pointing out. Firstly, the chromium distribution has a peak at 17 Å in both

structures. This peak is slightly higher for M_7C_3 compared to $M_{23}C_6$. While the chromium concentration is increased at the interface, the bulk ferrite matrix surrounding the precipitate has lowered levels of chromium. This can be seen as a dip between 22 Å and 25 Å in both Fig. 5.12a and b. No experimental or computational studies demonstrating this behavior have been found in the literature. However, this feature is on the order of 5 Å and is therefore too small to measure using experimental techniques as atom probe tomography [48]. Similar behavior has been observed in other systems with precipitates exhibiting core-shell structures [49]. The standard deviation for the model splits force predictions are low for all atoms in the structure further supporting that is authentic behavior, Fig.5.12.

Considering the distribution of vanadium in both systems in Fig. 5.12, there is little vanadium left in the carbide; instead, it has moved into the ferrite bulk. This is not unexpected, as iron-vanadium exhibits mixing, in the ferrite structure, at low vanadium concentration at the simulated temperature [50]. If the sites in the ferrite structure are energetically more favorable than those in the carbides, this would explain the behavior. The final metallic component, molybdenum, stays only in the carbide, a behavior expected for molybdenum, as it is not energetically favorable to mix into ferrite at 500 K [51].

Comparing the distribution of hydrogen in the carbide precipitates at 500 K, it is clear in both cases that hydrogen prefers the sites in the iron matrix surrounding the precipitate, as expected from experimental results. It is also evident that hydrogen diffuses into both structures to some extent. A larger amount of hydrogen diffuses into $M_{23}C_6$ than M_7C_3, it also permeates deeper, with significant levels of hydrogen found as far in as 8 Å. This implies that the diffusion paths in both structures enable hydrogen diffusion into the bulk, with the $M_{23}C_6$ pathways supporting diffusion further into the carbide bulk. It is worth noting that the prominence of the chromium peak decreases in $M_{23}C_6$ after the 15 ns MD run, from approximately 80% to 70%, and iron has also migrated further into the carbide. This suggests that high concentrations of hydrogen may affect the stability at the interface in $M_{23}C_6$, granting interface atoms higher mobility than before.

The average Voronoi volume for the structures at 500 K can be seen in Fig. 5.14a, where the hydrogen was extracted and the structure relaxed. In the bulk carbide, the result is similar to that of the volume per atom of carbide structures used in diffusivity calculations; $M_{23}C_6$ has a higher volume. Closer to the interface with the ferrite, the volume increases until it plateaus for $M_{23}C_6$, while M_7C_3 has a peak between 18 and 25 Å. Even without a volume peak, $M_{23}C_6$ is able to accommodate a similar amount of hydrogen in the same region, indicating that volume may not be important when differentiating between strong or weak hydrogen traps. Both carbides have a larger volume when inserted as a precipitate in the iron matrix compared to their bulk volume.

Increasing the temperature to 700 K, in Fig. 5.13, the behavior of hydrogen in both systems change. For both carbides there is a sharp decrease in the amount of hydrogen at the interface. More evenly distributed hydrogen for the higher temperature is expected as entropy will have a larger impact. This is more pronounced in the M_7C_3 structure where there is no longer a distinguishable peak, where as for $M_{23}C_6$ there still is. In the $M_{23}C_6$ case, there is also an additional peak inside the

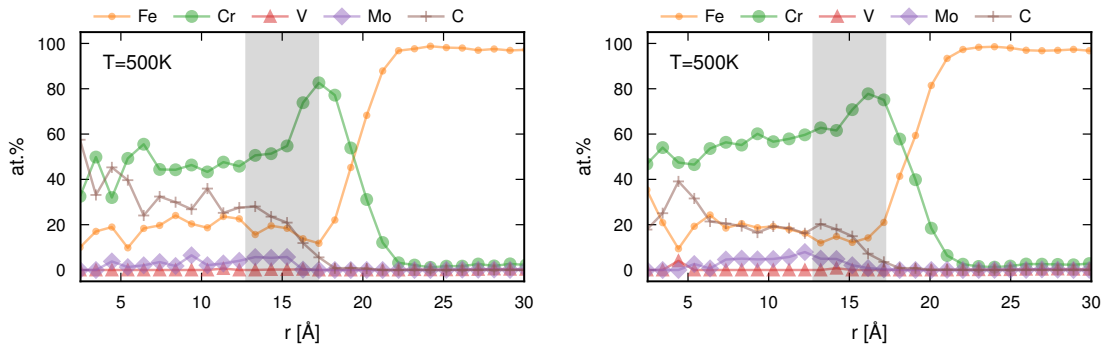

(a) M_7C_3 **(b)** $M_{23}C_6$

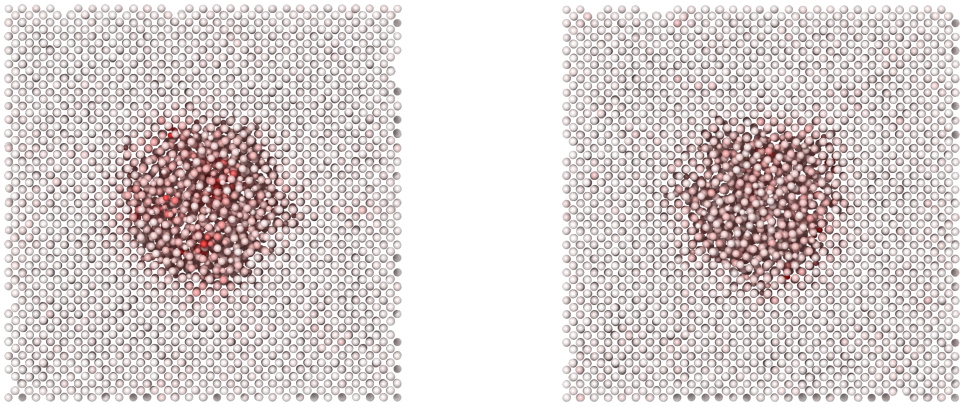

(c) M_7C_3 **(d)** $M_{23}C_6$

Figure 5.12: Distribution of metal species after equilibration using canonical MCMD allowing swapping between all metal species at 500 K. (a) M_7C_3 structure, and (b) $M_{23}C_6$ both with M=60%Cr, 20%Fe, 10%Mo, and 10%V. (c) And (d) force uncertainty in the equilibrated structures, the color indicates the uncertainty level for each atom and is the same in both structures. White colored atoms implies low uncertainty and red corresponds to the highest value (0.66 eV/Å).

bulk carbide at 12 Å. Between the two peaks in the outer regions of the carbide, the amount of hydrogen is increased compared to the initial 1% in the iron bulk, but still lower than in the two surrounding regions. The significant decrease in the interface region in the M_7C_3 precipitate indicate that in this region sites are not favorable enough for the hydrogen to stay trapped as the temperature increases. Instead entropic effects will start to dominate. Entropy should, and do, cause more hydrogen in the iron matrix and carbide bulk than at the interface. Considering the dimensionally of the interface compared to the bulk, 2D versus 3D, it is clear that configuration entropy should be higher in the bulk. The number of different possible configurations are higher in the bulk compared to the interface.

$M_{23}C_6$ has as mentioned two peaks in the hydrogen distribution, interface and carbide bulk, where there are sites that are energetically favorable enough to trap hydrogen even at the increased temperature. These sites are, in fact, the region seen in the diffusion simulations in Fig. 5.9. This supports that while the M_7C_3

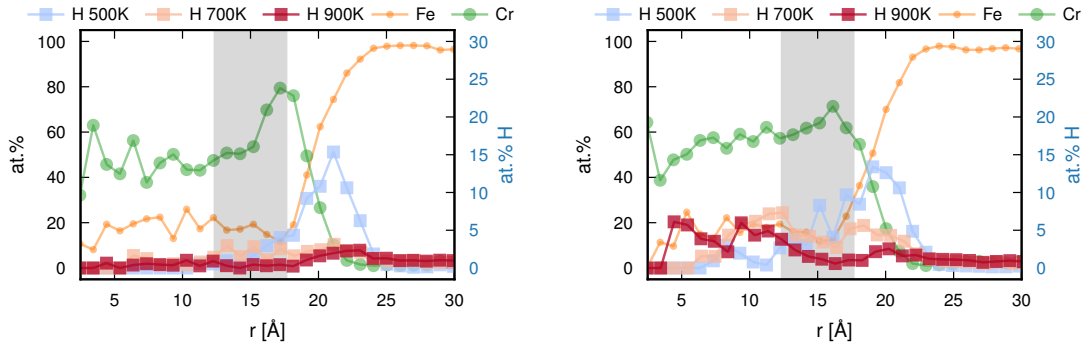

(a) M_7C_3 **(b)** $M_{23}C_6$

Figure 5.13: Distribution of iron, chromium, and hydrogen at three temperature after 15 ns MD simulations, due to the distribution of metal species being constant for the different temperature these are only plotted once. All hydrogen distributions are averaged over the last 2.5 ns. (a) M_7C_3 structure, and (b) $M_{23}C_6$ both with M=60%Cr, 20%Fe, 10%Mo, and 10%V.

has diffusion pathways through and into the carbide when the temperature is high enough for hydrogen to diffuse into the hydrogen there are few trapping sites that efficiently keep the hydrogen from participating in processes like HEDE and HELP. Instead the hydrogen is increasingly evenly distributed.

Calculating the Voroni volume for the higher temperature, see Fig. 5.14b, the difference between the two structure is almost identical to the lower temperatures. The only clear difference is that M_7C_3 no longer has a increased volume in the region surrounding the carbide, this may influence the absence of any distinguishable hydrogen peak. Also, $M_{23}C_6$ now has a higher volume than that of the ferrite in 7 Å to 12 Å, which aligns with the region of carbide with the highest hydrogen concentration. Further, the in the region where there is a valley in the hydrogen distribution there is a corresponding one in the average Voronoi volume. This may contribute to the levels of trapping or absence there of, however the effect is probably small consider the result for 500 K

At the highest simulated temperature 900 K, see Fig. 5.13, there are only slightly higher concentration of hydrogen at the interface for both structures. In the M_7C_3 the hydrogen is otherwise evenly spread throughout entire structure, both carbide and iron bulk have similar levels of hydrogenation. For $M_{23}C_6$ there are still sites that trap some hydrogen in the carbide bulk and near the interface, although to a lesser extent compared to 700 K. As previously, it is expected that the hydrogen is more evenly distributed, as temperature is increased, this is reflected in the results for both structures.

Considering instead Fig. 5.16 where the evolution of the hydrogen distributions over time is shown, each timestamp corresponds to the average distribution during 100 ps before and after. For both structures, and temperatures the first 2.5 ns is when most changes takes place and the final distribution is almost reached. This corresponds well with the timescales that should be expected for the hydrogen dif-

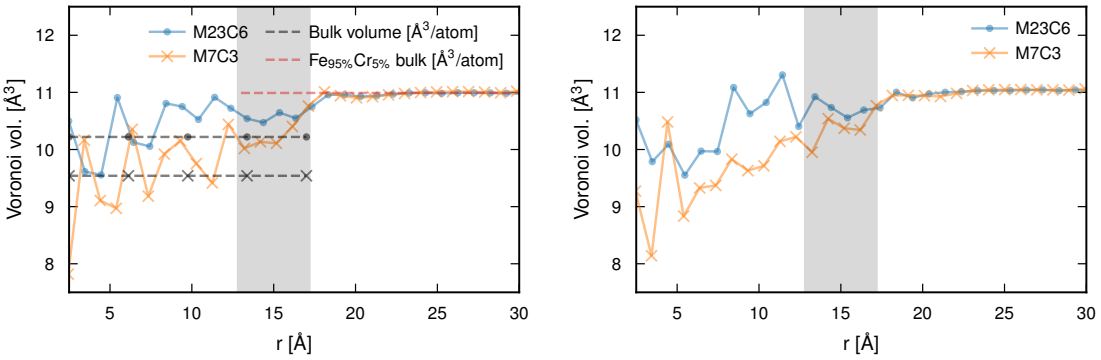

(a) 500 K **(b)** 700 K

Figure 5.14: Radial distribution of average Voronoi volume of relaxed interface M_7C_3 and $M_{23}C_6$ structures (M=60%Cr, 20%Fe, 10%V, and 10%Mo).

fusing through the ferrite matrix from diffusivity simulations discussed previously. This supports that the distribution in Fig. 5.13 are equilibrated and have reached a stable state. But there are some diffusion that seem to happen after this initial major redistribution of hydrogen from the ferrite bulk to interface.

At 500 K the M_7C_3 system does not change in a systematic way after 2.5 ns, instead the hydrogen is constantly focused at the ferrite-carbide interface. The concentration increasing only slightly from a peak of 14% to 15% in the next 2.5 ns. In the $M_{23}C_6$ system a similar behavior, where the largest change takes place in the first 2.5 ns, but there are some changes later as well. These later changes are focused in the interface region where more hydrogen diffuse into the carbide.

The 700 K simulation, see Fig. 5.16c and d, is similar to the 500 K case, although that there are fewer structured changes after the initial 2.5 ns. For $M_{23}C_6$ there is a slight drift towards the carbide core during the simulation, although this fluctuates for different times and might correspond to the hydrogen jumping in the energetically favorable regions identified in the diffusivity simulations.

For the highest temperature, 900 K in Fig. 5.16, there are only small changes in the M_7C_3 structure, with some hydrogen diffusing into the carbide bulk, but generally it is uniform. The $M_{23}C_6$ structure exhibits some interesting fluctuations in the hydrogen distribution inside the carbide bulk. This suggests that the hydrogen moves relatively freely when inside the carbide bulk.

Generally, the ferrite-carbide systems simulated in this section have similarities and differences both in the distribution of metallic components, final hydrogen distribution, and evolution of hydrogen over time. Firstly, for both structures, at the interface there is an increase in the concentration of chromium that is more prevalent in M_7C_3 compared to $M_{23}C_6$. Secondly, the $M_{23}C_6$ structure is shown to sustain more efficient diffusion into the carbide bulk, and also being able to trap larger amounts of hydrogen in the bulk compared to M_7C_3, Fig. 5.15. This can be related to the different diffusion processes that are present in the two carbides due to their structure and symmetries. At the higher temperatures the equilibrium hydrogen distribution seem to be governed mainly by entropy. Finally, for both carbides

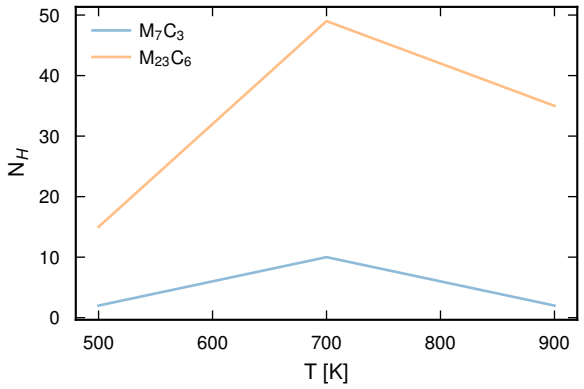

Figure 5.15: Number of hydrogen atoms within the carbide bulk, $r \leq 15\,\text{Å}$.

the hydrogen distribution evolves rapidly in the first 2.5 ns with the main features forming during that time, after this only minor changes happen to the distribution.

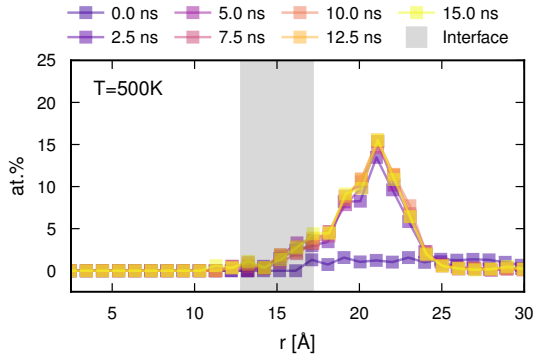

(a) M_7C_3 at 500 K

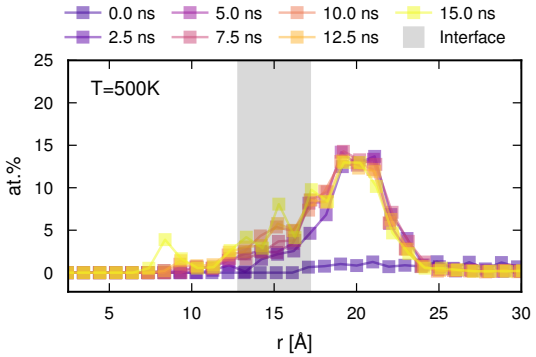

(b) $M_{23}C_6$ at 500 K

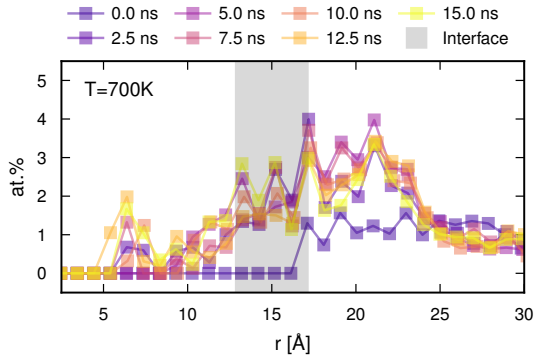

(c) M_7C_3 at 700 K

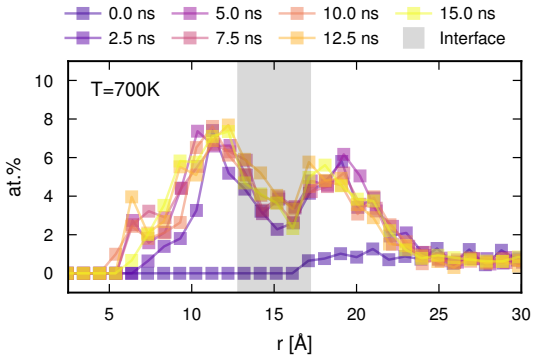

(d) $M_{23}C_6$ at 700 K

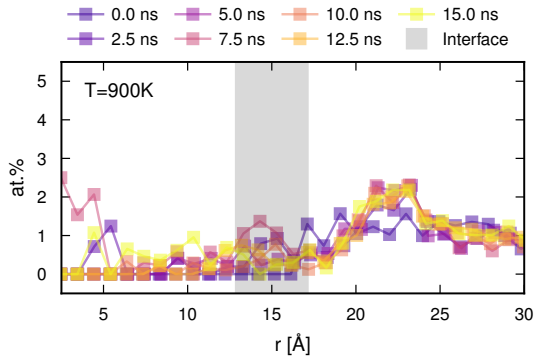

(e) M_7C_3 at 900 K

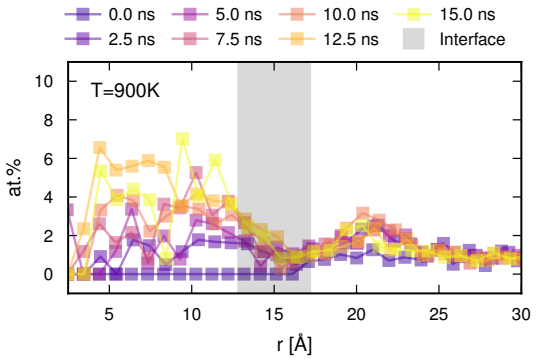

(f) $M_{23}C_6$ at 900 K

Figure 5.16: Radial distribution of H at different times in the interface region of a M_7C_3 and $M_{23}C_6$ (M=60%Cr, 20%Fe, 10%V, and 10%Mo) sphere encased in a 95%Fe5 %Cr volume at three different temperatures. And the interface between carbide and iron matrix is colored in gray.

6
Conclusion

In this work multiple different crystal structures have been studied using MD simulations: ferrite, both pure and with varying concentrations of chromium; M_7C_3 and $M_{23}C_6$ carbides with different compositions of metallic species: chromium, molybdenum, and vanadium; and finally, a combined system of ferrite with a carbide precipitate.

In ferrite, the chromium concentration influenced both the phase stability and hydrogen mobility. Monte Carlo simulations confirmed miscibility behavior in line with prior studies, while molecular dynamics simulations across five temperatures revealed that hydrogen diffusion follows a tetrahedral-to-tetrahedral mechanism. Although activation energies and diffusivity constants were somewhat overestimated, the trends matched experimental findings, with variations attributed to differing conditions between experiment and simulation.

Hydrogen diffusivity in M_7C_3-type carbides showed strong anisotropy, with preferred pathways aligned along cell channels. Among pure compositions, Fe_7C_3 exhibited the highest diffusivity but also showed signs of amorphization. Mixed-metal systems mitigated this anisotropy, offering additional diffusion paths. The energy barriers computed using NEB method showed good alignment between NEP and DFT reference. Notably, diffusivity in these carbides deviated from Arrhenius behavior, suggesting a strong temperature dependence for the elasticity of lattice. Correlation factor analysis showed a negative trend with increasing hydrogen content, though this effect diminished above 1100 K as hydrogen explored non-traditional pathways.

$M_{23}C_6$ was investigated in a manner similar to the M_7C_3 system, across all four metal species. The results showed that the $Fe_{23}C_6$ structure was unstable; in fact, even a 20% iron content in the bulk $M_{23}C_6$ system destabilized the entire structure at elevated temperatures. The remaining three pure carbides exhibited slightly lower diffusivity compared to their M_7C_3 counterparts. Unlike M_7C_3, their diffusivity was not anisotropic. In contrast to the well-defined diffusion pathways in M_7C_3, the $M_{23}C_6$ structure lacks clear channels. Instead of distinct pathways, $M_{23}C_6$ features regions of sites where hydrogen diffuses locally, with multiple paths connecting these regions. This behavior likely makes $M_{23}C_6$ less sensitive to defects and allows greater hydrogen diffusion into the bulk. Due to the complex unit cell, there are few ab initio studies on $M_{23}C_6$, and capturing this behavior requires larger structures and longer simulation times than what is feasible with DFT. As a result, comparable data is limited, and it is difficult to apply the NEB method for calculating diffusion barriers.

The correlation factor was also calculated for the $M_{23}C_6$ system, specifically in $Cr_{23}C_6$. While the M_7C_3 correlation factor had a initial decrease and then increas-

ing, for $M_{23}C_6$ it instead increases monotonically. At ten percent hydrogen, the diffusivity is three times higher than at one percent. This substantial increase is likely due to saturation of trapping sites, resulting in a larger proportion of hydrogen atoms remaining mobile.

In composite systems, both carbide types developed chromium-enriched shells at the ferrite interface, though the effect was more pronounced in M_7C_3. Hydrogen exposure destabilized the $M_{23}C_6$ shell, suggesting higher atomic mobility at its surface. Vanadium was spontaneously removed from the carbide phase during equilibration, consistent with its ability to mix into the ferrite at the studied temperature. However, since mixed-phase systems, of ferrite containing vanadium, were underrepresented in the training data, energy predictions for these configurations may be less accurate.

Hydrogen simulations in composite systems demonstrated that both M_7C_3 and $M_{23}C_6$ supports hydrogen trapping at the interface and within the carbide bulk, with the latter showing stronger and more thermally persistent trapping than M_7C_3. Despite its lower diffusivity, $M_{23}C_6$ seem to be a more effective hydrogen trap, especially in its ability to trap hydrogen in the bulk, a conclusion supported by recent experimental studies.

In summary, the questions raised at the beginning of this work regarding hydrogen behavior in ferrite-carbide systems have been addressed. With differences in diffusion mechanisms, trapping behavior, and structural stability between M_7C_3 and $M_{23}C_6$ being demonstrated. There are still many possible further areas of research. For this the $M_{23}C_6$ structure is especially relevant due to the lack of computational studies on its interactions with hydrogen. Such studies could identify the specific sites where hydrogen is trapped, and their solution energies, in $M_{23}C_6$ and the barriers between the regions of hydrogen sites. Also the behavior of the interface structure between carbide and ferrite can be studied further.

Bibliography

[1] R. P. Gangloff and B. P. Somerday, "Introduction," in *Gaseous Hydrogen Embrittlement of Materials in Energy Technologies*, R. P. Gangloff and B. P. Somerday, Eds. Woodhead Publishing, Jan. 2012, vol. 1, pp. xv–xix, ISBN: 978-0-85709-536-7. DOI: 10.1016/B978-0-85709-536-7.50018-0.

[2] R. Jones, "Gaseous hydrogen embrittlement of high performance metals in energy systems: Future trends," in *Gaseous Hydrogen Embrittlement of Materials in Energy Technologies*, R. P. Gangloff and B. P. Somerday, Eds. Woodhead Publishing, Jan. 2012, vol. 1, pp. 471–484, ISBN: 978-0-85709-536-7. DOI: 10.1533/9780857095374.3.471.

[3] G. Pressouyre, "Trap theory of hydrogen embrittlement," *Acta Metallurgica*, vol. 28, no. 7, pp. 895–911, Jul. 1980, ISSN: 0001-6160. DOI: 10.1016/0001-6160(80)90106-6.

[4] L. Vandewalle, T. Depover, and K. Verbeken, "Current state-of-the-art of hydrogen trapping by carbides: From theory to experiment," *International Journal of Hydrogen Energy*, Apr. 2024, ISSN: 0360-3199. DOI: 10.1016/j.ijhydene.2024.03.266.

[5] R. Salehin, G. B. Thompson, and C. R. Weinberger, "Hydrogen trapping and storage in the group IVB-VIB transition metal carbides," *Materials & Design*, vol. 214, p. 110 399, 2022, ISSN: 0264-1275. DOI: https://doi.org/10.1016/j.matdes.2022.110399.

[6] B. Zhang, J. Su, M. Wang, *et al.*, "Atomistic insight into hydrogen trapping at MC/BCC-Fe phase boundaries: The role of local atomic environment," *Acta Materialia*, vol. 208, p. 116 744, Apr. 2021, ISSN: 1359-6454. DOI: 10.1016/j.actamat.2021.116744.

[7] J. Li and C. Shi, "Carbides in special steel," in *Carbide in Special Steel: Formation Mechanism and Control Technology*, J. Li and C. Shi, Eds. Singapore: Springer Singapore, 2021, pp. 1–57, ISBN: 978-981-16-1456-9. DOI: 10.1007/978-981-16-1456-9_1.

[8] Z. Fan, Y. Wang, P. Ying, *et al.*, "GPUMD: A package for constructing accurate machine-learned potentials and performing highly efficient atomistic simulations," *Journal of Chemical Physics*, vol. 157, no. 11, p. 114 801, Sep. 21, 2022. DOI: 10.1063/5.0106617.

[9] Z. Fan, Z. Zeng, C. Zhang, *et al.*, "Neuroevolution machine learning potentials: Combining high accuracy and low cost in atomistic simulations and application to heat transport," *Physical Review B*, vol. 104, no. 10, p. 104 309, Sep. 2021. DOI: 10.1103/PhysRevB.104.104309.

[10] P. Y. Liu, B. Zhang, R. Niu, *et al.*, "Engineering metal-carbide hydrogen traps in steels," *Nature Communications*, vol. 15, p. 724, 2024. DOI: 10.1038/s41467-024-45017-4.

[11] W. Gerberich, "8 - modeling hydrogen induced damage mechanisms in metals," in *Gaseous Hydrogen Embrittlement of Materials in Energy Technologies*, R. P. Gangloff and B. P. Somerday, Eds. Woodhead Publishing, Jan. 2012, vol. 1, pp. 209–246, ISBN: 978-0-85709-536-7. DOI: 10.1533/9780857095374.2.209.

[12] J. P. Blackledge, "An introduction to the nature and technology of hydrides," in *Metal Hydrides*, W. M. Mueller, J. P. Blackledge, and G. G. Libowitz, Eds. Academic Press, Jan. 1968, pp. 1–20, ISBN: 978-1-4832-3215-7. DOI: 10.1016/B978-1-4832-3215-7.50005-8.

[13] J. Lee, T. Lee, D.-J. Mun, C. M. Bae, and C. S. Lee, "Comparative study on the effects of Cr, V, and Mo carbides for hydrogen-embrittlement resistance of tempered martensitic steel," *Scientific Reports*, vol. 9, no. 1, p. 5219, Mar. 2019, ISSN: 2045-2322. DOI: 10.1038/s41598-019-41436-2.

[14] D. E. Jiang and E. A. Carter, "Diffusion of interstitial hydrogen into and through BCC Fe from first principles," *Physical Review B*, vol. 70, no. 6, p. 064 102, Aug. 2004. DOI: 10.1103/PhysRevB.70.064102.

[15] A. Jacob, E. Povoden-Karadeniz, and E. Kozeschnik, "Revised thermodynamic description of the Fe-Cr system based on an improved sublattice model of the σ phase," *Calphad*, vol. 60, pp. 16–28, Mar. 2018, ISSN: 0364-5916. DOI: 10.1016/j.calphad.2017.10.002.

[16] A. Jain, S. P. Ong, G. Hautier, *et al.*, "Commentary: The materials project: A materials genome approach to accelerating materials innovation," *APL Materials*, vol. 1, no. 1, p. 011 002, Jul. 2013, ISSN: 2166-532X. DOI: 10.1063/1.4812323.

[17] A. M. Krause, P. A. Olsson, D. Music, and C. Bjerkén, "Interstitial diffusion of hydrogen in M7C3 (M=Cr,Mn,Fe)," *Computational Materials Science*, vol. 218, p. 111 940, Feb. 2023, ISSN: 0927-0256. DOI: 10.1016/j.commatsci.2022.111940.

[18] T. Depover and K. Verbeken, "Hydrogen trapping and hydrogen induced mechanical degradation in lab cast Fe-C-Cr alloys," *Materials Science and Engineering: A*, vol. 669, pp. 134–149, Jul. 2016, ISSN: 0921-5093. DOI: 10.1016/j.msea.2016.05.018.

[19] A. R. Allnatt and A. B. Lidiard, "The theory of random walks," in *Atomic Transport in Solids*. Cambridge: Cambridge University Press, 1993, pp. 317–336, ISBN: 978-0-521-54342-2. DOI: 10.1017/CBO9780511563904.010.

[20] A. R. Allnatt and A. B. Lidiard, "Atomic movements in solids – phenomenological equations," in *Atomic Transport in Solids*. Cambridge: Cambridge University Press, 1993, pp. 1–49, ISBN: 978-0-521-54342-2. DOI: 10.1017/CBO9780511563904.002.

[21] T.-T. Fang, M.-I. Chen, and W.-D. Hsu, "Insight into understanding the jump frequency of diffusion in solids," *AIP Advances*, vol. 10, no. 6, p. 065 132, Jun. 2020, ISSN: 2158-3226. DOI: 10.1063/5.0007178.

[22] C. Wert and C. Zener, "Interstitial atomic diffusion coefficients," *Physical Review*, vol. 76, no. 8, pp. 1169–1175, Oct. 1949. DOI: 10.1103/PhysRev.76.1169.

[23] C. Zener, "Theory of D_0 for atomic diffusion in metals," *Journal of Applied Physics*, vol. 22, no. 4, pp. 372–375, Apr. 1951, ISSN: 0021-8979. DOI: 10.1063/1.1699967.

[24] G. Murch, "The haven ratio in fast ionic conductors," *Solid State Ionics*, vol. 7, no. 3, pp. 177–198, Oct. 1982, ISSN: 0167-2738. DOI: 10.1016/0167-2738(82)90050-9.

[25] D. Porter, K. Easterling, and M. Sherif, *Phase Transformations in Metals and Alloys*. CRC Press, Sep. 2021, ISBN: 978-1-003-01180-4. DOI: 10.1201/9781003011804.

[26] R. G. Parr and Y. Yang Weitao, *Density-Functional Theory of Atoms and Molecules*. Oxford, UNITED STATES: Oxford University Press, Incorporated, 1994, ISBN: 978-0-19-535773-8. [Online]. Available: http://ebookcentral.proquest.com/lib/chalmers/detail.action?docID=4702301.

[27] M. E. Tuckerman, *Statistical mechanics: theory and molecular simulation*. Oxford university press, 2023.

[28] H. J. C. Berendsen, J. P. M. Postma, W. F. van Gunsteren, A. DiNola, and J. R. Haak, "Molecular dynamics with coupling to an external bath," *The Journal of Chemical Physics*, vol. 81, no. 8, pp. 3684–3690, Oct. 1984, ISSN: 0021-9606. DOI: 10.1063/1.448118.

[29] M. Bernetti and G. Bussi, "Pressure control using stochastic cell rescaling," *The Journal of Chemical Physics*, vol. 153, no. 11, p. 114 107, Sep. 2020, ISSN: 0021-9606. DOI: 10.1063/5.0020514.

[30] G. Bussi, D. Donadio, and M. Parrinello, "Canonical sampling through velocity rescaling," *The Journal of Chemical Physics*, vol. 126, no. 1, p. 014 101, Jan. 2007, ISSN: 0021-9606. DOI: 10.1063/1.2408420.

[31] B. Sadigh and P. Erhart, "Calculation of excess free energies of precipitates via direct thermodynamic integration across phase boundaries," *Phys. Rev. B*, vol. 86, p. 134 204, 13 Oct. 2012. DOI: 10.1103/PhysRevB.86.134204.

[32] B. Sadigh, P. Erhart, A. Stukowski, A. Caro, E. Martinez, and L. Zepeda-Ruiz, "Scalable parallel monte carlo algorithm for atomistic simulations of precipitation in alloys," *Phys. Rev. B*, vol. 85, p. 184 203, 18 May 2012. DOI: 10.1103/PhysRevB.85.184203.

[33] G. Henkelman and H. Jónsson, "Improved tangent estimate in the nudged elastic band method for finding minimum energy paths and saddle points," *The Journal of Chemical Physics*, vol. 113, no. 22, pp. 9978–9985, Dec. 2000, ISSN: 0021-9606. DOI: 10.1063/1.1323224.

[34] G. Henkelman, B. P. Uberuaga, and H. Jónsson, "A climbing image nudged elastic band method for finding saddle points and minimum energy paths," *The Journal of Chemical Physics*, vol. 113, no. 22, pp. 9901–9904, Dec. 2000, ISSN: 0021-9606. DOI: 10.1063/1.1329672.

[35] E. Lindgren *et al.*, "Calorine: A python package for constructing and sampling neuroevolution potential models," *Journal of Open Source Software*, vol. 9, no. 95, p. 6264, 2024. DOI: 10.21105/joss.06264.

[36] M. Ångqvist, W. A. Muñoz, J. M. Rahm, *et al.*, "ICET – a python library for constructing and sampling alloy cluster expansions," *Advanced Theory and Simulations*, vol. 2, no. 7, p. 1 900 015, 2019. DOI: https://doi.org/10.1002/adts.201900015. eprint: https://onlinelibrary.wiley.com/doi/pdf/10.1002/adts.201900015.

[37] A. Hjorth Larsen, J. Jørgen Mortensen, J. Blomqvist, *et al.*, "The atomic simulation environment—a python library for working with atoms," *Journal of Physics: Condensed Matter*, vol. 29, no. 27, p. 273 002, Jun. 2017, ISSN: 0953-8984. DOI: 10.1088/1361-648X/aa680e.

[38] A. Stukowski, "Visualization and analysis of atomistic simulation data with ovito–the open visualization tool," *Modelling and Simulation in Materials Science and Engineering*, vol. 18, no. 1, p. 015 012, Dec. 2009, ISSN: 0965-0393. DOI: 10.1088/0965-0393/18/1/015012.

[39] A. Togo, K. Shinohara, and I. Tanaka, "Spglib: A software library for crystal symmetry search," *Science and Technology of Advanced Materials: Methods*, vol. 4, no. 1, p. 2 384 822, Dec. 2024. DOI: 10.1080/27660400.2024.2384822.

[40] E. Bitzek, P. Koskinen, F. Gähler, M. Moseler, and P. Gumbsch, "Structural relaxation made simple," *Physical Review Letters*, vol. 97, no. 17, p. 170 201, Oct. 2006. DOI: 10.1103/PhysRevLett.97.170201.

[41] Kuwano and Hisashi, "Mössbauer effect study on the miscibility gap of the iron-chromium binary system," *Transactions of the Japan Institute of Metals*, vol. 26, no. 7, pp. 473–481, 1985. DOI: 10.2320/matertrans1960.26.473.

[42] I. Peñalva, G. Alberro, F. Legarda, R. Vila, and C. Ortiz, "Influence of Cr content on the diffusive transport parameters and trapping of hydrogen in Fe alloys," *Proceedings of the 11th International Symposium on Fusion Nuclear Technology-11 (ISFNT-11) Barcelona, Spain, 15-20 September, 2013*, vol. 89, no. 7, pp. 1628–1632, Oct. 2014, ISSN: 0920-3796. DOI: 10.1016/j.fusengdes.2014.04.018.

[43] Y. Hayashi and W. Shu, "Iron (ruthenium and osmium)-hydrogen systems," *Solid State Phenomena*, vol. 73–75, pp. 65–114, 2000, ISSN: 1662-9779. DOI: 10.4028/www.scientific.net/SSP.73-75.65.

[44] C. M. Fang, M. A. van Huis, and H. W. Zandbergen, "Structural, electronic, and magnetic properties of iron carbide Fe_7C_3 phases from first-principles theory," *Physical Review B*, vol. 80, no. 22, p. 224 108, Dec. 2009. DOI: 10.1103/PhysRevB.80.224108.

[45] P. Ghosh, K. Ali, A. Vineet, A. Voleti, and A. Arya, "Study of structural, mechanical and thermal properties of θ-Fe3C, o-Fe7C3 and h-Fe7C3 phases using molecular dynamics simulations," *Journal of Alloys and Compounds*, vol. 726, pp. 989–1002, Dec. 2017, ISSN: 0925-8388. DOI: 10.1016/j.jallcom.2017.08.058.

[46] C. M. Fang, M. H. F. Sluiter, M. A. van Huis, C. K. Ande, and H. W. Zandbergen, "Origin of predominance of cementite among iron carbides in steel at elevated temperature," *Physical Review Letters*, vol. 105, no. 5, p. 055 503, Jul. 2010. DOI: 10.1103/PhysRevLett.105.055503.

[47] C. Fang, M. van Huis, M. Sluiter, and H. Zandbergen, "Stability, structure and electronic properties of γ-Fe23C6 from first-principles theory," *Acta Ma-*

terialia, vol. 58, no. 8, pp. 2968–2977, May 2010, ISSN: 1359-6454. DOI: 10.1016/j.actamat.2010.01.025.

[48] M. K. Miller, "Field ion microscopy," in *Atom Probe Tomography: Analysis at the Atomic Level*, M. K. Miller, Ed. Boston, MA: Springer US, 2000, pp. 45–83, ISBN: 978-1-4615-4281-0. DOI: 10.1007/978-1-4615-4281-0_3.

[49] S. Cheng, T. Hou, D. Zhang, *et al.*, "New insights into the formation mechanism of the multicomponent carbides (Nb, M)C (M = Ti, Cr and Mn)," *Journal of Materials Research and Technology*, vol. 28, pp. 1022–1031, Jan. 2024, ISSN: 2238-7854. DOI: 10.1016/j.jmrt.2023.11.179.

[50] S. M. Dubiel and J. Cieślak, "Sigma-phase in Fe-Cr and Fe-V alloy systems and its physical properties," *Critical Reviews in Solid State and Materials Sciences*, vol. 36, no. 4, pp. 191–208, Oct. 2011, ISSN: 1040-8436. DOI: 10.1080/10408436.2011.589232.

[51] A. F. Guillermet, "The Fe-Mo (iron-molybdenum) system," *Bulletin of Alloy Phase Diagrams*, vol. 3, no. 3, pp. 359–367, Dec. 1982, ISSN: 0197-0216. DOI: 10.1007/BF02869315.

DEPARTMENT OF PHYSICS
CHALMERS UNIVERSITY OF TECHNOLOGY
Gothenburg, Sweden
www.chalmers.se

CHALMERS
UNIVERSITY OF TECHNOLOGY